Characteristics of Kelvin-Helmholtz Waves as Observed by the MMS from September 2015 to March 2020

Rachel C Rice[1,1], Katariina Nykyri[1,1], Xuanye Ma[1,1], and Brandon Lee Burkholder[1,1]

[1]Embry-Riddle Aeronautical University

November 30, 2022

Abstract

The Magnetospheric Multiscale (MMS) mission has presented a new opportunity to study the fine scale structures and phenomena of the Earth's magnetosphere, including cross scale processes associated with the Kelvin-Helmholtz Instability (KHI), but such studies of the KHI and its secondary processes will require a database of MMS encounters with Kelvin-Helmholtz (KH) waves. Here we present an overview of 45 MMS observations of the KHI from September 2015 to March 2020. Growth rates and unstable solid angles for each of the 45 events were calculated using a new technique to automatically detect plasma regions on either side of the magnetopause boundary. There was no apparent correlation between solar wind conditions during the KHI and its growth rate and unstable solid angle, which is not surprising as KH waves were observed downstream of their source region. We note all KHI were observed for solar wind flow speeds between 295 km/s and 610 km/s, likely due to a filtering effect of the instability onset criteria and plasma compressibility. Two-dimensional Magnetohydrodynamic (2D MHD) simulations were compared with two of the observed MMS events. Comparison of the observations with the 2D MHD simulations indicates that the new region sorting method is reliable and robust. The ability to automatically detect separate plasma regions on either side of a moving boundary and determine the KHI growth rate may prove useful for future work identifying and studying secondary processes associated with the KHI.

Characteristics of Kelvin-Helmholtz Waves as Observed by the MMS from September 2015 to March 2020

Rachel Rice[1], Katariina Nykyri[1], Xuanye Ma[1], Brandon Burkholder[2]

[1]Embry-Riddle Aeronautical University, Department of Physical Sciences, Center for Space and Atmospheric Research

[2]University of Maryland Baltimore County, Goddard Planetary Heliophysics Institute

Key Points:

- A survey of MMS data from September 2015 to March 2020 identified 45 Kelvin-Helmholtz wave events.
- Events are observed for the full range of solar wind conditions. Growth rates are independent of solar wind conditions.
- A new method is developed for the automatic detection of magnetosheath and magnetospheric regions within the KHI.

Corresponding author: Rachel Rice, ricer4@my.erau.edu

Abstract

The Magnetospheric Multiscale (MMS) mission has presented a new opportunity to study the fine scale structures and phenomena of the Earth's magnetosphere, including cross scale processes associated with the Kelvin-Helmholtz Instability (KHI), but such studies of the KHI and its secondary processes will require a database of MMS encounters with Kelvin-Helmholtz (KH) waves. Here we present an overview of 45 MMS observations of the KHI from September 2015 to March 2020. Growth rates and unstable solid angles for each of the 45 events were calculated using a new technique to automatically detect plasma regions on either side of the magnetopause boundary. There was no apparent correlation between solar wind conditions during the KHI and its growth rate and unstable solid angle, which is not surprising as KH waves were observed downstream of their source region. We note all KHI were observed for solar wind flow speeds between 295 km/s and 610 km/s, likely due to a filtering effect of the instability onset criteria and plasma compressibility. Two-dimensional Magnetohydrodynamic (2D MHD) simulations were compared with two of the observed MMS events. Comparison of the observations with the 2D MHD simulations indicates that the new region sorting method is reliable and robust. The ability to automatically detect separate plasma regions on either side of a moving boundary and determine the KHI growth rate may prove useful for future work identifying and studying secondary processes associated with the KHI.

1 Introduction

The ways in which the solar wind (SW) couples to the Earth's magnetosphere and its impacts on local space weather is a fundamental question of space physics. Several mechanisms operating at the magnetopause boundary, such as magnetic reconnection [*Paschmann et al.*, 1979; *Sonnerup et al.*, 1981; *Gosling et al.*, 1986; *Burch and Phan*, 2016] and viscous interactions [*Axford and Hines*, 1961; *Otto and Fairfield*, 2000; *Fairfield et al.*, 2000], are responsible for the transfer of mass and energy from the solar wind to the magnetosphere. Understanding the detailed effects of these processes is vital to predict and help prevent negative outcomes from space weather. Consider as an example, the dawn-dusk asymmetry of the magnetosphere plasma sheet.

Observations from Defense Meteorological Satellite Program (DMSP) and Time History of Events and Macroscale Interactions during Substorm (THEMIS) spacecraft have established that the cold component ions of the plasma sheet are 30-40% hotter in the dawn flank than in the dusk [*Hasegawa et al.*, 2003; *Wing et al.*, 2005]. *Dimmock et al.* [2015] conducted a statistical study of the magnetosheath source population as observed by THEMIS spacecraft over seven years, which showed ions in the dawn flank are on average 10-15% hotter than those in the dusk flank. This asymmetry is more pronounced under fast ($>$ 400 km/s) SW conditions [*Dimmock et al.*, 2015]. However, even during fast SW, the asymmetry of the magnetosheath source plasma is insufficient to produce the observed asymmetry in the plasma sheet. MHD simulations were unable to reproduce the observed sheath asymmetry, but it was apparent in hybrid models, suggesting a kinetic scale mechanism is responsible for asymmetrically driving the heating of cold component ions in the sheath [*Dimmock et al.*, 2015].

Several physical mechanisms have been proposed as drivers of the observed plasma sheet asymmetry. The Kelvin-Helmholtz instability (KHI), which occurs regularly at the magnetopause boundary, is one such mechanism [*Otto and Fairfield*, 2000; *Fairfield et al.*, 2000; *Nykyri et al.*, 2003; *Hasegawa et al.*, 2004; *Nykyri et al.*, 2006; *Taylor et al.*, 2008; *Foullon et al.*, 2008; *Merkin et al.*, 2013; *Lin et al.*, 2014; *Ma et al.*, 2014a,b; *Nykyri et al.*, 2017; *Ma et al.*, 2017; *Sorathia et al.*, 2019]. The KHI occurs in regions of large shear flow [*Chandrasekhar*, 1961], such as the boundary between the shocked SW (the magnetosheath) and the relatively stagnant magnetosphere [*Miura and Pritchett*, 1982]. Long established as a source for momentum and energy transport from the SW to the magnetosphere [*Miura*, 1984, 1987], later simulations and observations have shown non-linear stages of the KHI are also capable of reconnection and mass transport [*Nykyri and Otto*, 2001, 2004; *Nykyri et al.*, 2006; *Hasegawa et al.*, 2009] and ion heating via kinetic wave modes within the vortex [*Moore et al.*, 2016, 2017]. Compressional waves, like Kelvin-Helmholtz or ultra-low frequency (ULF) waves, can also lead to kinetic Alfvén wave (KAW) generation via mode conversion [*Johnson et al.*, 2001; *Chaston et al.*, 2007]. Recent work by *Nykyri et al.* [2021] has suggested that KAWs associated with the KHI can contribute to parallel electron heating, but in that case, were insufficient to account for the total observed electron heating. Identifying the detailed mechanism or mechanisms driving electron scale waves within the KHI and quantifying their contribution to electron heating is still an open question.

Observations have shown the KHI may form on both the dawn and dusk flanks under any orientation of the interplanetary magnetic field (IMF) [*Kavosi and Reader*, 2015], but simulations have shown a preference for dawn flank formation when the IMF is in a Parker Spiral (PS) orientation [*Nykyri*, 2013; *Adamson et al.*, 2016]. Work by *Henry et al.* [2017] analyzed the events presented in *Kavosi and Reader* [2015] and confirmed this preference observationally. *Henry et al.* [2017] also confirmed a preference for KHI formation at the dusk flank for high solar wind speeds under northward IMF (NIMF). As PS is the most statistically common IMF orientation, it follows that the associated preference for dawn-side KHI development would also be statistically more common. Such asymmetry in the formation of KHI, combined with Kelvin-Helmholtz (KH) driven secondary processes like reconnection and kinetic scale waves, make the KHI a strong candidate to drive the dawn-dusk asymmetry of cold-component ions in the plasma sheet.

The launch of the Magnetospheric Multiscale (MMS) satellites presents a new opportunity to extend this study of the KHI and its associated secondary processes to smaller scales with higher resolution measurements. Within months of its launch, MMS had encountered KHI [*Eriksson et al.*, 2016]. The event reported by *Eriksson et al.* [2016] has been the subject of several case studies: *Li et al.* [2016] found evidence of Alfvénic ion jets and electron mixing due to reconnection at the trailing edge of the vortex; *Wilder et al.* [2016] noted compressed current sheets and evidence of ion-acoustic waves, and *Stawarz et al.* [2016] took advantage of MMS's high temporal and spatial resolutions to study turbulence generated by the KHI. These secondary processes would contribute to ion heating and plasma transfer across the magnetopause boundary.

Case studies are useful in identifying the fine-scale secondary processes associated with the KHI, but statistical studies are necessary to fully understand their role and quantify their contribution to heating and driving the plasma sheet asymmetry. It is therefore imperative, as a first step, to build a database of MMS encounters with KHI. Comparison of the location, duration, and prevailing IMF conditions of many events with the growth rates and unstable solid angles can help establish patterns which may prove informative in understanding the role KHI plays in magnetospheric dynamics (e.g., in generating dawn-dusk asymmetries via secondary, "cross-scale" processes or affecting the radiation belt electron populations via ULF wave generation or magnetopause shadowing).

In this paper we present a list of MMS encounters with the KHI and the physical characteristics of each, which may be used for future studies of small scale secondary processes. The MMS instrumentation and observational signatures used to identify the KHI encounters are described in Section 2.1 and 2.2, respectively. Growth rates and the unstable solid angle used to characterize the KHI are derived in Section 2.3 . Section 2.4 details the methodology used to separate magnetosheath and magnetospheric regions of the observed events, in order to caclulate the growth rates and unstable solid angle for each event. Results of these calculations are presented in Section 3. The methodology was also tested using 2-dimensional magnetohydrodynamic simulations as described in Section 4. Conclusions are presented and discussed in Section 5.

2 Methodology

2.1 MMS Instrumentation

Observational data reported here is level 2 survey data from MMS1 [*Burch et al.*, 2016]. Spacecraft separations are at most 230 km, and most often between 20 and 50 km, well below the typical size of the KHI, thus all spacecraft are expected to observe the same signatures and a single craft is sufficient to identify the KHI. Ion energy spectra and ion and electron moments are taken from the Fast Plasma Investigation (FPI) [*Pollock et al.*, 2016]. The Flux Gate Magnetometer (FGM) provides the DC magnetic field [*Russell et al.*, 2016; *Torbert et al.*, 2016]. Data file versions used are v3.3.0.cdf for FPI and v4.18.0.cdf for FGM. SW data are taken from the OMNI database [*King and Papitashvili*, 2005].

2.2 Observational Signatures & Identification of the KHI

Between September 2015 and March 2020, MMS made thousands of full and partial crossings of the magnetopause. In order to narrow the search field, we limited ourselves to magnetopause crossings which were noted to be unstable in the MMS event database. Approximately 100 unique intervals were tagged as potentially containing KHI activity. These crossings were checked by eye to determine if they exhibited the characteristics of the KHI. These characteristic signatures are as follows:

- Quasi-periodic fluctuations in omnidirectional ion energy;

When MMS crosses a stable magnetopause boundary, we expect to see a smooth transition from plasma with energy typical of the magnetosheath to plasma with typical magnetospheric energy (or vice versa). When the boundary is not stable, this transition will not be smooth, and may show alternating regions of plasma with energies typical of the magnetosheath and magnetosphere, as well as mixed energies due to plasma mixing in the KH vortex. For the case of a boundary disturbed by a periodic instability like the KHI, these alternating regions should also be relatively periodic.

- Quasi-periodic, anti-correlated fluctuations in ion density and temperature;

The periodic observation of the magnetosheath and mangetospheric regions will also be evident in the ion density and temperature, as MMS alternately encounters regions of plasma from the cold, dense magnetosheath and the hot, tenuous magnetosphere.

- Velocity shear(s) on the order of 100s of km/s;

Large velocity shears are common at the flank magentopause, where the magnetosphere is relatively stagnant and the magnetosheath plasma is accelerating from low speeds immediately after the shock to "catch up" with the SW speed further downtail [*Dimmock and Nykyri*, 2013]. Large velocity shears are also a necessary condition for the development of the KHI [*Chandrasekhar*, 1961; *Miura*, 1984, 1987].

- Fluctuations in the total magnetic field;

The total strength of the magnetic field will vary as the KH vortex compresses the field lines.

- Bipolar variations in the normal component of the magnetic field

Fluctuations in the magnetic field should appear as bipolar variations in the normal component as the vortex twists the field lines. Changes in the normal component and total magnetic field help distinguish the KHI from a shifting boundary, such as a response to SW dynamic pressure variations.

- Fluctuations in total pressure, specifically decreases corresponding to the center of the KH vortex, where $\mathbf{B_N}$ is near 0.

The rotational nature of the KHI creates an outward force which is balanced by a pressure gradient, resulting in a decrease of total pressure at the center of the vortex. KHI events thus show a lower total pressure near the center of the vortex (where B_N is zero) and higher pressure in the spine region. This signature allows us to distinguish the KHI from a flux transfer event (FTE) in which total pressure typically increases when B_N is zero [*Nykyri et al.*, 2006; *Zhao et al.*, 2016]. We note that MMS will not always observe this particular signature, depending on the path MMS takes through the instability.

Twisting at the boundary is also evident in a comparison of the normal component with the total bulk velocity. At a quiet boundary, plasma bulk velocity is generally tangential to the boundary. As a KHI twists the boundary, the normal component of the velocity increases. We compare the maximum absolute value of the normal velocity component to the total velocity at the time of observation. For a well developed vortex, the maximum value of the normal velocity should be a significant fraction of the total velocity. The ratio of the maximum normal velocity to the total velocity for each event is presented in Section 3

To obtain the normal component of the field, observed magnetic field data is rotated into boundary normal (LMN) coordinates using the maximum variance of the electric field (MVA-E) technique. The general method for variance analysis techniques is given in *Sonnerup and Scheible* [1998]. *Nykyri et al.* [2011a,b] showed the single spacecraft MVA-E technique is sufficient for identification of the boundary normal direction when the plasma bulk velocity and magnetic field are primarily tangential to the boundary, as is typically the case during KHI. It is also used here, rather than a multi-spacecraft method, to allow for automation of the analysis. For MVA-E, the direction in which the convective $(\mathbf{v} \times \mathbf{B})$ electric field variance is maximized (i.e., the direction of the maximum eigenvector of the variance matrix) is taken as the normal direction, $\mathbf{N}$. The 180° ambiguity in the normal direction is resolved by requiring the unit normal be positive pointing outward from the magnetosphere. Tangential directions, $\mathbf{L}$ and $\mathbf{M}$, are defined by the intermediate and minimum eigenvectors of the MVA-E matrix, but are not relevant to the current analysis.

All of the above signatures are present in the two example cases shown in Figures 1 and 2. The first five signatures are present in all identified events listed in Table 1. The final signature is dependent on the MMS trajectory through the KHI, and may or may not be visible in the observational data for any given event.

Figure 1 shows MMS1 survey level observations from 06:00 to 07:00 UT on 15 October 2015, the availability of burst mode data for portions of the interval is indicated with a blue bar at the top of the figure. MMS passed through the dusk flank of the dayside magnetopause during strongly duskward IMF. The omni-directional ion energy spectrogram in panel (a) shows the expected quasi-periodic variations throughout the interval, which are well matched by anti-correlated changes in ion density and temperature (c). A velocity shear on the order of 200 km/s is visible near 06:26 UT in panel (d). The GSM magnetic field in panel (e) shows 20-40nT fluctuations characteristic of the KHI from 06:26 to 06:39 UT and again near from 06:48 to 06:55 UT. These fluctuations are also present as bipolar variations in the normal component of the magnetic field (f). Decreases in total pressure (g) are visible starting around 06:27 UT and continuing through 06:48 UT. The decreases of total pressure correspond with times at which the normal magnetic field component is near 0, particularly from 06:35-06:40 UT.

Survey mode MMS1 observations of another KHI encounter from 16:35 to 19:07 UT on 26 September 2017 are shown in Figure 2. The blue bar at top again indicates burst mode data is available for portions of the interval. MMS crossed the dusk flank tail magnetopause while the IMF was in a PS orientation with a strong northward component. Quasi-periodic fluctuations in omni directional ion spectra are observable throughout the interval in panel (a) and are accompanied by anti-correlated variations in ion density and temperature (c). Velocity shears (d) on the order of 200 km/s occur regularly throughout the interval. Panel (e) shows fluctuations around 10 nT in the total magnetic field, which are also visible as bipolar signatures in the normal component of the magnetic field (f). Decreases in total pressure (g) of approximately 0.1 nPa correspond well with times when BN is near 0.

Table 1 summarizes the 45 MMS encounters with the KHI between September 2015 and March 2020. In this time period MMS observed more KH events on the dusk side magnetopause (29) than on the dawn-side (16). Events are evenly distributed between the dayside and tail magnetopause: 22(23) events occur sunward(tailward) of the terminator. KHI in the tail are all observed in or after May 2017, which is primarily due to a sampling effect of the MMS orbit change from Phase One, which targeted the dayside magnetopause, to Phase Two, which targeted the tail. The observed events ranged in duration from as little as 10 minutes to nearly 13 hours. Burst mode data is available for portions of all 45 events, which will be useful for future studies of smaller scale processes within the KHI.

SW data from OMNI is available for 44 of the 45 events, which occur under a variety of IMF orientations and solar wind conditions. We consider the planar and B_Z components separately. At the time at which MMS first observes the KHI, the planar components of the IMF show a preference for PS (17). Less common are radial, duskward, dawnward (8 each), and ortho-Parker Spiral (OPS) (3) orientations. For the duration of each event, the planar components of the average IMF configurations show a preference for the PS orientation (17), followed by radial and dawnward (8 each) orientation. Duskward (6) and OPS (5) orientations are less common. At event onset, the $\mathbf{B_Z}$ component of the IMF was more often northward (27) than southward (17). This preference for NIMF orientation holds true for the duration of each event: 26 (18) of the events occurred under average $\mathbf{B_Z}$ positive (negative). The IMF vectors and values of the SW conditions for each event are available in the Supplement. SW parameters are discussed and correlated with KHI growth rates in Section 3.

Having identified MMS encounters with the KHI, we next calculate the growth rate and unstable solid angle of each event and compare the results with the prevailing solar wind and IMF properties.

2.3 Instability Growth Rate & Unstable Solid Angle

Assuming an infinitely thin boundary layer, a region unstable to the KHI will satisfy the KH instability criteria

$$[\mathbf{k} \cdot (\mathbf{v_1} - \mathbf{v_2})]^2 \geq \frac{n_1 + n_2}{4\pi m_0 n_1 n_2}[(\mathbf{k} \cdot \mathbf{B_1})^2 + (\mathbf{k} \cdot \mathbf{B_2})^2] \tag{1}$$

where $\mathbf{v_i}$, n_i, and $\mathbf{B_i}$ are the the velocity, density, and magnetic field on either side of the velocity shear layer and $\mathbf{k}$ is the wave vector [*Chandrasekhar*, 1961].

Equation 1 may be rearranged to determine the normalized growth rate of the KHI in a particular region, which is defined as

$$Q/k = \sqrt{a_1 a_2 (\mathbf{\Delta v} \cdot \hat{\mathbf{k}})^2 - a_1 (\mathbf{v_{A1}} \cdot \hat{\mathbf{k}})^2 - a_2 (\mathbf{v_{A2}} \cdot \hat{\mathbf{k}})^2} \tag{2}$$

where a_i is a density parameter for either side of the boundary, defined by $a_i = \rho_i/(\rho_1 + \rho_2)$, $\mathbf{v_{Ai}}$ is the Alfvén velocity, and $\hat{\mathbf{k}}$ is the unit wave vector (thus the growth rate is normalized to the wavelength), pointing in the direction of maximum growth. We use only

Table 1. The date, onset time, duration, GSM location, and estimated wavelength of 45 KHI events observed by MMS from September 2015 to March 2020. Burst mode data is available for portions of all events.

Event Number, Date	Onset Time [UT]	Duration [min]	GSM Location [R_E]	KH Wave-length [R_E]	Event Number, Date	Onset Time [UT]	Duration [min]	GSM Location [R_E]	KH Wave-length [R_E]
01, 08-Sep-15	09:00	170	[5.0, 7.4, -4.5]	2.80	24, 19 May-17	23:58	107	[-17.8, -16.6, -2.1]	20.72
02, 15-Sep-15	10:45	240	[5.1, 8.7, -5.5]	5.00	25, 20 May-17	02:00	150	[-17.6, -17.4, -0.6]	26.65
03, 11-Oct-15	10:30	30	[8.7, 6.5, -4.7]	3.71	26, 20 Sep-17	22:32	43	[-10.8, 20.9, 1.3]	8.20
04, 15-Oct-15	06:00	60	[9.0, 4.1, -2.3]	2.29	27, 26 Sep-17	16:35	152	[-9.3, 19.6, -0.9]	6.47
05, 17-Oct-15	16:00	28	[6.4, 7.8, -4.1]	4.94	28, 16 Oct-17	14:30	50	[-4.0, 18.6, -2.7]	7.71
06, 18-Oct-15	15:00	25	[7.2, 7.5, -4.4]	8.18	29, 30 Oct-17	19:05	35	[-0.6, 17.3, 1.6]	4.20
07, 22-Dec-15	22:15	35	[7.9, -5.7, -1.8]	2.58	30, 02 Nov-17	17:25	50	[-0.9, 14.8, 0.8]	6.38
08, 11-Jan-16	20:52	18	[6.2, -7.6, -3.4]	1.99	31, 03 May-18	00:15	35	[-9.3, -17.5, -2.3]	8.43
09, 19-Jan-16	19:57	38	[5.3, -8.2, -3.9]	3.25	32, 18 Sep-18	15:50	25	[-14.1, 20.6, -1.0]	5.17
10, 05-Feb-16	18:55	35	[3.3, -9.3, -5.0]	5.97	33, 24 Sep-18	14:10	195	[-14.1, 20.3, -1.6]	19.35
11, 07-Feb-16	03:45	55	[7.0, -6.9, -3.5]	4.20	34, 02 Oct-18	23:45	35	[-10.8, 22.5, 2.1]	11.25
12, 18-Feb-16	19:30	70	[2.5, -9.7, -6.3]	6.81	35, 04 Oct-18	17:25	10	[-0.8, 16.2, -0.2]	2.50
13, 25-Feb-16	18:55	70	[1.3, -9.9, -6.5]	2.26	36, 13 Apr-19	07:45	30	[-0.6, -17.5, 2.4]	9.68
14, 26-Sep-16	14:15	70	[2.7, 8.5, -5.4]	11.85	37, 03 Jun-19	23:05	75	[-2.2, -14.9, -3.8]	7.46
15, 27-Sep-16	19:50	20	[0.3, 11.5, -3.4]	2.62	38, 25 Sep-19	13:45	765	[-16.7, 22.0, -0.2]	12.33
16, 04-Oct-16	18:20	70	[1.8, 11.2, -3.6]	9.51	39, 02 Oct-19	08:15	165	[-9.9, 21.5, -4.5]	8.54
17, 10-Oct-16	14:40	60	[4.3, 9.3, -5.0]	9.43	40, 02 Oct-19	16:00	80	[-12.9, 23.5, -2.1]	13.03
18, 24-Oct-16	10:50	30	[6.8, 6.1, -4.3]	1.09	41, 02 Oct-19	21:40	25	[-14.6, 24.0, 1.1]	7.11
19, 04-Nov-16	11:45	75	[8.1, 7.2, -3.8]	2.28	42, 06 Oct-19	14:50	175	[-14.8, 24.4, -4.2]	17.10
20, 03-May-17	02:00	150	[-12.9, -19.7, -3.9]	17.39	43, 15 Oct-19	19:00	75	[1.2, 12.8, 2.9]	8.81
21, 08-May-17	13:00	110	[-14.8, -17.2, 0.3]	11.50	44, 22 Oct-19	22:00	20	[1.8, 15.3, 3.8]	3.76
22, 11-May-17	12:00	150	[-15.6, -18.2, 1.4]	18.47	45, 12 Nov-19	20:30	75	[6.7, 11.8, 5.2]	7.04
23, 11-May-17	15:44	31	[-15.3, -19.2, -0.3]	7.75					

proton data to determine the values in Equation 2 as the low mass electrons have no meaningful influence on the growth rate, and minor ion species are not abundant enough to contribute significantly.

Note Equation 2 is an upper limit of the growth rate for an observed event due to the assumption of an infinitely thin boundary, which is not true for the magnetopause. Equations 1 and 2 also assume an incompressible plasma, yet for very high (> 600 km/s) SW speeds, the compressibility is generally sufficient to stabilize the development of the KHI. Due to these assumptions, the growth rate as determined by Equation 2 is an overestimate of the growth rate for an observed KHI. It must also be noted that MMS is unlikely to observe the source region of the KHI and local conditions may not match those of the source region. The difference in growth rate from the source region to the observation point is not predictable from observations.

In order to compare the growth rates for KHI events observed at various locations and under a variety of SW and IMF conditions, we make it unitless via normalization to the local fast mode speed, $v_{fm} = \sqrt{v_A^2 + c_s^2}$. Both magnetic tension and compressibility have stabilizing effects on the KHI. Likewise, the fast mode speed is dependent on magnetic tension via the Alfvén velocity, v_A, and compressibility via the sound speed, c_s. Further, *Miura and Pritchett* [1982] showed the KHI growth rate is strongly correlated to the fast mode speed, and is stable for $Q/k > v_{fm}$, thus it is more physically meaningful to normalize to the fast mode speed than another characteristic speed.

It is also important to note, our expression of the fast mode speed here is an upper limit which assumes the magnetic field is perpendicular to the bulk velocity. When the field and velocity are parallel, the larger of the sound or Alfvén speed is used as the fast mode speed. This means the unitless growth rate we present is a lower bound, and may be larger depending upon the relative geometry of the magnetic field and bulk velocity.

The fast mode speed is not equal in the magnetosheath (sub-index msh) and magnetosphere (sub-index msp), so we normalize to the mean of the two, such that

$$Q_{unitless} = \frac{Q/k}{v_{fm}}$$

where $v_{fm} = \frac{1}{2}(v_{fmmsh} + v_{fmmsp})$.

In Equation 2 the direction of $\hat{\mathbf{k}}$ is chosen to maximize the normalized growth rate, but many directions of $\hat{\mathbf{k}}$ may satisfy the instability criteria. This range of angles capable of satisfying the instability criteria can be used to determine just how susceptible a region is to the development of the KHI.

The KHI may propagate in any direction $\hat{\mathbf{k}}$ for which Q/k is real (the right hand side of Equation 2 is positive under the square root). If we express $\hat{\mathbf{k}}$ in terms of the spherical angles ϕ and θ, the percent of the 4π solid angle that satisfies the KHI instability criteria at a given location may be calculated. We term this percentage the "unstable solid angle" [*Burkholder et al.*, 2020; *Nykyri et al.*, 2021]. Events with larger unstable solid angles are likely to be KHI.

Growth rate alone is not a sufficient parameter to characterize the KHI; cases with small growth rates can be indicative of a source region further upstream, such that the KHI has already created a more diffuse boundary layer. The KHI is a convective instability which dissipates stored energy as it develops, thus growth rate and the unstable solid angle are maximized just prior to the formation of the KH vortex. The nature of in-situ observations, however, dictates we cannot identify a KHI until it is relatively well developed. Thus small growth rates and unstable solid angles are not necessarily counter-indicative of the presence of the KHI, but may instead be features of later stage KH waves.

As a secondary check for events with low growth rates, we plot tailward velocity as a function of density to see if the KHI vortex had rolled over, examples of which are seen in Figure 3. As the KHI develops, it may form non-linear vortices in which low density magnetospheric plasma becomes trapped and is dragged tailward with magnetosheath-like velocities. This is seen in observations as low density plasma (typically associated with the magnetosphere) flowing tailward with the magnetosheath [*Hasegawa et al.*, 2006; *Taylor et al.*, 2012], and is apparent as points in the lower left quadrant of Figure 3. For the 15 October 2015 event, ions do not show signatures of roll-over, indicating the KHI is in an earlier phase of development. For the 26 September 2017 event, ions with magnetosphere-like density flowing with magnetosheath-like velocities are present, indicating the KHI has rolled over to form a well-developed vortex.

Another indicator of vortex roll-over within the KHI is a comparison of the normal component with the total bulk velocity. At a quiet boundary, plasma bulk velocity is generally tangential to the boundary. As a KHI twists the boundary, the normal component of the velocity increases. We compare the maximum absolute value of the normal velocity component to the total velocity at the time of observation. For a well developed vortex, the maximum value of the normal velocity should be a significant fraction of the total velocity.

Results for the growth rate, unitless growth rate, unstable solid angle, and relative value of normal velocity are presented in Section 3.

2.4 Automated Region Sorting

Calculation of the growth rate and unstable solid angle requires the identification of separate regions of magnetosheath and magnetospheric plasma on either side of the magnetopause boundary. This is made difficult by the plasma mixing inherent within KH waves. In case studies it is common to select a few minutes of data in the pure magnetosheath and magnetosphere regions well away from the unstable boundary area. This is not, however, the most robust or efficient way to handle region identification for the many cases necessary for a statistical study. Instead, we seek to automate the process of separating the magnetosheath and magnetosphere regions.

The unperturbed flank magnetosheath is characterized by cold, dense plasma flowing tailward at high speeds with the shocked SW. In contrast the magnetospheric plasma near the flanks is hot, tenuous, and relatively stagnant. Thus, a combination of density, temperature, and the X-component of the bulk velocity may be used to separate data from the magnetosheath and magnetosphere regions. The isolated data provides the mean values of density, velocity, etc. in each region which are used in the calculation of the growth rates and unstable solid angle.

The magnetosheath is identified by the product of ion density and tailward velocity divided by the average ion temperature, nv_{tail}/T. The GSM$-X$ velocity component, v_X, is measured to be large and negative in the sheath and small, either positive or negative, in the magnetosphere. To simplify our parameter, we shift the tailward velocity to be strictly positive with a minimum value at 0, such that $v_{tail} = |v_X - \max(v_X)|$. The resulting parameter, nv_{tail}/T, is thus large in the magnetosheath and small in the magnetosphere. We identify the sheath as any region in which the value of nv_{tail}/T is greater than 1.5 times the magnetopause value. The magnetopause value is defined as the mean of the largest 12.5% and smallest 12.5% of all nv_{tail}/T values (for a total of

25% of available data) for each event. This method allows us to reliably identify the magnetosheath regions near the KHI while avoiding the inclusion of mixed and transition regions in our calculations of the KHI growth rate and unstable solid angle (see the Supplementary Information for details justifying the data ranges and cutoff values presented here).

The nv_{tail}/T parameter does not, however, reliably isolate magnetospheric plasma. Instead, we use the ion specific entropy, $S = T/n^{2/3}$, to identify magnetospheric regions within each KHI event. The hot, tenuous magnetosphere has much higher specific entropy than the magnetosheath, so we may follow the same procedure as employed for isolating the magnetosheath with specific entropy in place of the nv_{tail}/T parameter to separate the magnetosphere. That is, any region with specific entropy 1.5 times greater than the magnetopause value is considered to be the magnetosphere. Again the magnetopause value is the mean of the largest 12.5% and smallest 12.5% (25% total) of all entropy values for the event. This allows for reliable determination of the magnetospheric regions near the KHI without including mixed and transition plasma regions (see Supplementary Information).

The results of this region sorting method are are depicted in panel b of Figures 1 and 2. Red (blue) bars represent regions of magnetosphere (magnetosheath) plasma. The green bar identifies regions of mixed plasma. In both example events, the identified regions are in good agreement with omnidirectional ion energy spectrograms and the ion density and temperature measurements. In Figure 3 red and blue points also represent the magnetosphere and magnetosheath respectively. In the 2017 case, rolled-over plasma is considered mixed, despite having density more characteristic of the magnetosphere. This is a good indicator that our method of automatically separating regions is selecting only pure magnetosheath and magnetospheric plasmas and excluding regions where the KHI has already caused mixing.

Having isolated the separate regions, we then calculate mean values of density, temperature, velocity, and magnetic field on either side of the boundary. These values are checked to ensure they fall within typical ranges for the magnetosheath and magnetosphere before they are used in calculation of the growth rate and unstable solid angle. The new method was also tested using simulation data, and provided good agreement with known values (see Section 4 and Supplementary Information).

3 Observational Results

Having separated the magnetosheath and magnetospheric regions of each event, growth rates (GR), unitless growth rates (UGR), and unstable solid angles (USA) are calculated. Results for all 45 events are listed in Table 2. GR range from 3.93 to 103.16 km/s. When normalized to the fast mode speed, UGR range from 0.005 to 0.325, but more typically are between 0.010 and 0.200. That is, the KHI typically develops at 1-20% of the local fast mode speed; only 1 event falls below this range and 7 above it. USA range from 0.06 to 39.51. At its maximum, the normal component of velocity often accounts for more than 60%, and occasionally all, of the total velocity, indicating the observed KH waves have significantly twisted the boundary. Events with strongly twisted boundaries are good candidates for future studies of reconnection and other secondary processes driven by the KHI.

GR, UGR, and USA show some dependence on location, as can be seen in Figure 4. The locations of the KHI events observed by MMS are plotted in the GSM X-Y (left column), X-Z (middle column), and Y-Z (right column) planes and color coded according to the GR (top row), UGR (middle row), and USA (bottom row). KHI observed near the sub-solar point tend to have lower GR than those observed further along the magnetopause, particularly those observed along the tail. This is still apparent even when growth rates are normalized to the local fast mode speeds. This is likely due to the low velocity shear near the subsolar point. Immediately after the bow shock, the magnetosheath plasma is slowed significantly from SW speeds, and the shear between the sheath and magnetosphere is much lower than further downtail, where the magnetosheath plasma has accelerated and returned to values of SW velocity. The low velocity shear near the subsolar point will result in lower GR and UGR, as can be seen from Equation 2.

USA shows a similar pattern as the GR and UGR, with larger values observed further down tail. Again, this can be explained by the large velocity shears encountered along the tail magnetopause. On the dayside, the shocked solar wind of the magnetosheath is still accelerating back up to SW speed after encountering the obstacle of earth's magnetosphere and bow shock, thus velocity shears between the sheath and magnetosphere are smaller. Further down tail, the magnetosheath plasma has re-achieved the high SW flow speed, thus increasing the shear between the two regions. For larger velocity shears,

Table 2. Growth rates (GR), unitless growth rates (UGR), unstable solid angles (USA), and the relative value of the maximum normal velocity component for each of the 45 KHI events observed by MMS from September 2015 to March 2020. At its maximum, the normal velocity component is a significant fraction of the total velocity for most events. The asterisk indicates the high-latitude event studied by *Nykyri et al.* [2021] and *Michael et al.* [2021]

Event Number, Date	GR [km/s]	UGR	USA [%]	v_{Nmax} $/v_{tot}$	Event Number, Date	GR [km/s]	UGR	USA [%]	v_{Nmax} $/v_{tot}$
01, 08-Sep-15	81.63	0.081	6.37	0.96	24, 19-May-17	90.54	0.186	29.00	0.93
02, 15-Sep-15	16.27	0.019	0.82	0.99	25, 20-May-17	47.42	0.066	30.22	0.75
03, 11-Oct-15	15.68	0.016	0.42	0.58	26, 20-Sep-17	53.99	0.145	18.75	0.19
04, 15-Oct-15	8.83	0.007	0.11	0.85	27, 26-Sep-17	52.01	0.189	24.23	0.83
05, 17-Oct-15	25.05	0.032	4.01	0.92	28, 16-Oct-17	26.03	0.047	6.74	0.79
06, 18-Oct-15	52.31	0.063	9.07	0.83	29, 30-Oct-17	11.51	0.023	4.70	0.97
07, 22-Dec-15	10.41	0.010	0.29	0.83	30, 02-Nov-17	39.55	0.109	5.95	0.67
08, 11-Jan-16	17.47	0.015	0.27	0.89	31, 03-May-18	95.59	0.325	23.37	0.97
09, 19-Jan-16	13.78	0.025	0.12	0.52	32, 18-Sep-18	40.87	0.090	9.96	0.91
10, 05-Feb-16	22.31	0.028	5.74	0.93	33, 24-Sep-18	71.16	0.227	36.91	0.73
11, 07-Feb-16	13.36	0.019	0.16	0.66	34, 02-Oct-18	41.17	0.111	10.18	0.65
12, 18-Feb-16	34.90	0.038	8.96	1.00	35, 04-Oct-18	31.26	0.081	6.16	0.50
13, 25-Feb-16*	5.01	0.012	0.08	0.69	36, 13-Apr-19	48.93	0.089	15.66	0.76
14, 26-Sep-16	51.46	0.068	7.26	0.99	37, 03-Jun-19	42.25	0.108	16.63	0.94
15, 27-Sep-16	84.07	0.117	8.37	0.96	38, 25-Sep-19	74.22	0.198	28.04	0.91
16, 04-Oct-16	54.67	0.063	7.17	0.70	39, 02-Oct-19	29.28	0.083	6.10	0.58
17, 10-Oct-16	43.30	0.059	8.98	0.75	40, 02-Oct-19	96.46	0.209	26.71	0.82
18, 24-Oct-16	3.93	0.005	0.06	0.71	41, 02-Oct-19	37.12	0.111	18.09	0.52
19, 04-Nov-16	16.78	0.019	0.78	0.95	42, 06-Oct-19	82.43	0.210	34.49	0.98
20, 03-May-17	56.65	0.197	39.51	0.85	43, 15-Oct-19	94.08	0.296	18.37	0.98
21, 08-May-17	84.15	0.278	29.87	1.00	44, 22-Oct-19	52.52	0.110	12.00	1.00
22, 11-May-17	45.56	0.103	12.07	0.87	45, 12-Nov-19	103.16	0.250	14.34	0.90
23, 11-May-17	49.99	0.198	13.33	0.33					

the stabilizing effects of the magnetic field are less influential in the development of KHI, and a larger solid angle is thus unstable to the growth of the KHI.

A cluster of KHI events occur at high southern magnetic latitudes (GSM-Z $< -4.5R_E$), showing the KHI is not limited to lower latitudes. This is a new finding, as previous missions, such as THEMIS, remained at lower magnetic latitudes. Only three prior studies, two using Cluster data [*Hwang et al.*, 2012; *Ma et al.*, 2016], and one using MMS data [*Nykyri et al.*, 2021; *Michael et al.*, 2021] (marked with asterisk in Table 2), have been conducted on the KHI at high latitudes near the dawn and dusk flanks of the high-altitude cusps.

Figure 5 depicts the GR (top), UGR (middle), and USA (bottom), of 44 of the 45 events as a function of SW density (far left), temperature (center left), flow speed (center), Alfvén Mach number (center right), and IMF magnitude (far right) taken from OMNI data. OMNI data was not available for one event. The color bar indicates the event number, so each event is shown with the same color in all plots for direct comparison.

SW density ranges from 2.6 to 17.0 /cc. Observed events are well distributed over the density range, and no relationship is apparent between density and GR or USA. Temperatures generally range from 0.7 to 31.4 eV, with one outlier event occurring with a SW temperature of 61.0 eV. Most events are observed for SW temperatures less than 20 eV, but no trend in GR, UGR, or USA is apparent.

There is an apparent selection window in the solar wind flow speed, with all events occurring when solar wind flow is between 295 and 610 km/s. This fits with expectations that low velocity shears between the sheath and magnetosphere are not unstable to the KHI, and compressibility effects for very large shears stabilize the KHI [*Miura and Pritchett*, 1982]. Within this selection window there is no correlation between SW flow speed and GR, UGR, or USA. Alfvén Mach numbers also show no clear relationship to GR, UGR, or USA. Events are observed for Alfvén Mach numbers between 3.8 and 26.3, though most events occur when the Mach Number is below 20.

IMF magnitude for all but one event is greater than 1.5 nT and less than 11.2 nT. The outlier event occurred for an average IMF magnitude of 20.8 nT [*Eriksson et al.*, 2016]. Events are otherwise evenly distributed throughout the range of IMF magnitudes with no apparent relationship to GR, UGR or USA.

We also compare the solar wind conditions for which KHI is observed to the solar wind conditions throughout the entire 4.5 year interval from September 2015 to March 2020 in Figure 6. MMS observes KHI for the full range of solar wind conditions. Density, temperature, flow speed, and Alfvén Mach number values during KH intervals occur with similar frequency as in the full time range with only slight deviations. The most pronounced difference is in SW flow speed. KHI intervals overrepresent high SW speeds, particularly between 350 and 450 km/s. This is unsurprising, as KH develop preferentially for high ($>$ 400 km/s) SW speeds and compressibility at very high speeds ($>$ 600 km/s) can have a stabilizing effect. Given the distribution of SW speeds during the 4.5 year interval, the apparent selection window in SW speed is probably not significant, as the solar wind speed is not often below 300 km/s or above 600 km/s.

As can be seen in Figure 7, IMF magnitude during KH intervals is nearly identical to the observations in the complete time range, with a small decrease around the most common strength and an increase at very large IMF (this is due to the outlier event occurring for IMF $\approx$ 20 [*Eriksson et al.*, 2016]). The planar IMF components show no significant or conclusive variation from the full time range to the KHI intervals. For the B_Z component of the IMF, KHI intervals tend to occur more for NIMF than southward IMF (SIMF). This is likely due to subsolar reconnection during SIMF, which creates a more diffuse boundary layer which is less prone to the development of the KHI.

The SW conditions and IMF orientations help explain the observation of more KHI on the dusk side of the magnetopause than on the dawn side. *Henry et al.* [2017] found dusk flank formation to be more common both for high SW speeds ($>$ 400 km/s) and NIMF orientations. 25 of the 45 events occur when SW speed was high, and 29 of the 45 events had IMF orientations with positive B_Z components.

4 Comparison with Simulations

To verify our method of isolating regions on either side of the boundary is robust, it was applied to parameters generated by two dimensional MHD simulations of the KHI. A simulation case for a KHI developing under NIMF conditions was tested using initial conditions comparable to those of the event on 08 September 2015. A second simulation case used initial conditions similar to those of the 18 October 2015 event for the KHI developing on the dusk flank under Parker Spiral IMF (PSIMF) orientation.

The simulations, after *Ma et al.* [2019], solve the full set of resistive Hall-MHD equations using a leapfrog scheme [*Potter*, 1973; *Birn*, 1980; *Otto*, 1990]. We normalize all physical quantities to their typical scale, for example, the length L is normalized to L_0, the half width of the initial sheared flow; number density to n_0, the magnetic field to B_0, velocity to the Alfvén velocity, $v_A = B/\sqrt{\mu_0 \rho_0}$; and the time to the Alfvén transit time $T_A = L_0/v_A$. Exact values of the normalizations for both simulation cases are listed in the Supplement.

A cut is taken through the simulation box at every time step. Data from these cuts are separated into distinct regions using the method described in Section 2.4, then used to calculate GR and USA. The GR as a function of time is shown in blue in panel (a) of Figures 8 and 9 for the NIMF and PSIMF cases respectively. The GR of the observation case on which the simulations are based is also shown in black, and the simulation GR, as determined by the slope of the linear portion a plot of $\ln(v_\perp)$ as a function of time, is shown in green. Examples of the density at various time steps show the development of the KHI (panels b-f). The cuts used for calculations are shown in red in the same panels.

As can be seen in Figures 8 and 9, the KHI growth rate increased from its initial value until the cut through the simulation captured vortex roll-over. After roll-over is observed, growth rate decreases sharply then increases towards its initial level as the instability dissipates. All of this is consistent with expectations: the free energy available to drive the KHI peaks before the vortex forms. The KHI then dissipates the energy.

In the NIMF case, GR calculated using Equation 2 are significantly greater than the simulation GR. This is to be expected as Equation 2 assumes an infinitely thin boundary layer and incompressible plasma; the simulation GR is free from these assumptions. In contrast, the simulation GR is larger, though very near, than the GR determined using Equation 2 for the PSIMF case. This may be due to other assumptions made in the simulation (e.g. pressure is not constant, beta is smaller than observed).

Within the first few time steps, the simulation matches well with the observed GR for the NIMF case. The GR of the event the NIMF simulation is based on is 81.63 km/s. The initial GR for the simulation is 82.74 km/s, and remains within 5 km/s of the observed GR for more than 80 time steps. That is, the first 20% of the simulation is in rough agreement with the observation.

The PSIMF simulation shows equally good, if not better, agreement with the observed event on which it is based. The observed event has a GR of 52.41 km/s, and the initial GR value for the simulation is 52.44 km/s. The GR of the simulation remains within 5 km/s of the observation's GR for more than 230 time steps, or nearly 60% of the simulation.

We note the growth rate is dependent upon the geometry of the cut. The method of separating the two regions works best when the spacecraft spends a significant portion of the event duration on both sides of the boundary. Therefore, events in which MMS only skims the KHI or spends significantly more time in one region than the other may actually grow faster than our calculations would indicate. The dependence of GR on cut geometry are discussed in more detail in the Supplementary Information.

5 Conclusions and Discussion

The main conclusions may be summarized as follows:

- MMS observed 45 clear KHI events from September 2015 to March 2020.

From September 2015 to March 2020 MMS observed more than 100 unique mixed regions which initially resembled the KHI. Further analysis of total pressure and boundary-normal rotated magnetic field showed 45 of these events likely to be the KHI. These 45 events, summarized in Table 1, occur under a variety of prevailing SW conditions and IMF orientations.

The 45 events presented here form the beginnings of a database for statistical studies of the KHI and its associated secondary processes. Burst mode data is available for portions of all the identified events. This is useful and necessary for future studies of secondary processes approaching the electron scale. The methods used here may also be applied to the MMS data from April 2020 to present to further extend the database of events for analysis.

- An automated method uses nv_{tail}/T and specific entropy to identify the magnetosheath and magnetospheric regions, respectively, within a KH wave event. This method consistently isolates the pure regions, and excludes mixed plasma, both for real satellite and simulated data.

The identified magnetosheath and magnetospheric regions of each KHI event match well with the omni-directional ion energy spectrogram and density and temperature time series. Mean values of density, temperature, velocity, and magnetic field in the identified regions are consistent with expectations. Plots of the GSM$-X$ velocity and density show mixed regions are successfully avoided. See the Supplementary Information for more details on the development of the presented method and rejected alternatives.

In simulations the density within the identified regions throughout the simulation is within 0.15/cc of the initial value for the NIMF case and 0.25/cc of the initial value for the PSIMF case. Thus our method of isolating the pure magnetosheath and magnetosphere is reliable and robust even for late stage KHI with roll-over and mixing.

When comparing the results of the simulation and the observation, we see good agreement for the growth rate for the NIMF and PSIMF case. GR from the NIMF simulation was within 5 km/s agreement with the observational case for $\approx 20\%$ of the simulation, and the PS simulation was in agreement for nearly 60% of the simulation.

- Plasma parameters from the automatically isolated regions were used to calculate KHI GR, UGR, and USA for the 45 KHI events in our database.

GR, UGR normalized to the local fast mode speed, and USA for the 45 KHI events in our database are reported in Table 2.

Growth rates range from a minimum of 3.93 to 103.16 km/s. When normalized to the fast mode speed, the unitless growth rate ranges from 0.005 to 0.325 in the extremes, with most events in the 0.01 to 0.20 range. That is, most of the observed KHI grow at a speed that is between 1% and 20% of the local fast mode speed.

Two of the events have unstable solid angles less than 1% of the total 4π solid angle. Unstable solid angles are between 1% and 10% for 23 events, and between 10% and 25% for 17 events. Three events have unstable solid angles greater than 25% of the total 4π solid angle. Larger solid angles are more common further down tail where the velocity shear from the magnetosheath to the magnetosphere is greater and thus the stabilizing effects of the magnetic field are less influential.

We note a few of the observed events occur in apparently stable regions with very low growth rates (e.g: the high-latitude case on 25 Feb 2016 [*Nykyri et al.*, 2021; *Michael* *et al.*, 2021]; this does not preclude the observed events from being the KHI. Convective instabilities, like the KHI, dissipate energy stored in unstable regions and systems. As excess energy is dissipated, the region becomes more stable, thus maximum instability and growth rates occur just prior to the formation of the instability. Because it is difficult to identify the KHI in observational data until is relatively well developed and has dissipated some of the excess free energy, observations will only be made after growth rates have decreased from their maxima. We believe those events occurring in apparently more stable regions may be later in development than faster growing KHI in less stable areas.

We also note the path MMS takes through the KHI event can have a significant effect on the growth rate determination. Encounters which merely skim the KH vortex rather than passing directly through it may actually grow faster than our calculations would indicate.

- The KHI is observed when SW flow speeds are between 295 and 610 km/s. Within this flow speed selection window, KHI GR, UGR, and USA are independent of prevailing SW conditions.

Values of the GR, UGR, and USA for each event are listed in Table 2. As can be seen in Figure 5, GR, UGR, and USA appear to be independent of SW conditions, with the exception of SW flow speed. All of the observed events occurred when the SW speed was between 295 and 610 km/s. At flow speeds much below 295 km/s the velocity shear is too low to satisfy the KHI onset conditions (Equation 1). At SW speeds above 610 km/s the compressibility of the plasma will usually stabilize the KHI [*Miura and Pritchett*, 1982]. Within this selection window between 295 and 610 km/s however, flow speed is not correlated with GR, UGR, or USA. However, as can be seen in Figure 6, this selection window may reflect the distribution of SW speed throughout the entire 4.5 year time range considered in this study.

The database of MMS KHI observations presented here will be used in future studies of secondary processes associated with the KHI. The availability of burst mode data for all 45 events allows studies of secondary KHI processes to be extended to smaller spatial and temporal scales. The trends we have observed in the location and SW and IMF conditions may also be used to simplify the search for and identification of future KHI events.

Acknowledgments

Funding for this work was provided by the National Science Foundation under grant number 1707521 and by NASA under grants numbers NNZ17AI50G and NNX16AF89G. Thanks are owed to the entire MMS team, and especially to the FGM and FPI instrument groups. MMS data was retrieved from the MMS Science Data Center at lasp.Colorado.edu/mms/sdc/public. OMNI solar wind data is available from NASA Goddard Space Flight Center's Space Physics Data Facility at omniweb.gsfc.nasa.gov.

References

Adamson, E., K. Nykyri, and A. Otto (2016), The Kelvin-Helmholtz instability under Parker-spiral interplanetary magnetic field conditions at the magnetospheric flanks, *Advances in Space Research*, *58*.

Axford, W., and C. Hines (1961), A unifying theory of high-Latitude phenomena and geomagnetic storms, *Canadian Journal of Physics*, *39*, 1433–1464.

Birn, J. (1980), Computer studies of the dynamic evolution of the geomagnetic tail, *Journal of Geophysical Research*, *85*, 1214–1222.

Burch, J. L., and T. D. Phan (2016), Magnetic reconnection and the dayside magnetopause: advances with MMS, *Geophysical Research Letters*, *43*, 8327–8338, doi:10.1002/2016GL069787.

Burch, J. L., T. E. Moore, R. B. Torbert, and B. L. Giles (2016), Magnetospheric Multiscale overview and science objectives, *Space Science Reviews*, *199*, 5–21, doi:10.1007/s11214-015-0164-9.

Burkholder, B. L., K. Nykyri, X. Ma, R. Rice, S. A. Fuselier, K. J. Trattner, K. R. Pritchard, J. L. Burch, and S. M. Petrinec (2020), Magnetospheric multiscale observation of an electron diffusion region at high latitudes, *Geophysical Research Letters*, *47*(15), doi:10.1029/2020GL087268.

Chandrasekhar, S. (1961), *Hydrodynamic and Hydromagnetic Stability*, Oxford University Press.

Chaston, C. C., M. Wilber, M. Fujimoto, M. L. Goldstein, M. Acuna, H. Réme, and A. Fazakerley (2007), Mode conversion of anomalous transport in Kelvin-

Helmholtz vortices and kinetic Alfvén waves at Earth's magnetopause, *Physical Review Letters*, *99*.

Dimmock, A. P., and K. Nykyri (2013), The statistical mapping of magnetosheath plasma properties based on THEMIS measurements in the magnetosheath interplanetary medium reference frame, *Journal of Geophysical Research*, *118*, 4963–4876.

Dimmock, A. P., K. Nykyri, H. Karimabadi, A. Osmane, and T. I. Pulkkinen (2015), A statistical study into the spatial distribution and dawn-dusk asymmetry of dayside mangetosheath ion temperatures as a function of upstream solar wind conditions, *Journal of Geophysical Research*, *120*, 2767–2782, doi:10.1002/2014JA020734.

Eriksson, S., B. Lavraud, F. D. Wilder, J. E. Stawarz, B. L. Giles, J. L. Burch, W. Baumjohann, R. E. Ergun, P.-A. Lindqvist, W. Magnes, C. J. Pollock, C. R. Russel, Y. Saito, R. J. Strangeway, R. B. Torbert, D. J. Gershmann, Y. V. Khotyaintsev, J. C. Dorelli, S. J. Schwartz, L. Avanov, E. Grimes, Y. Vernisses, A. P. Sturner, T. D. Phan, G. T. Marklund, T. E. Moore, W. R. Paterson, and K. A. Goodrich (2016), Magnetospheric multiscale observations of magnetic reconnection associated with Kelvin-Helmholtz waves, *Geophysical Research Letters*, *43*, 5606–5615, doi:10.1002/2016GL068783.

Fairfield, D. H., A. Otto, T. Mukai, S. Kokubun, R. P. Lepping, J. T. Steinberg, A. J. Lazaurs, and T. Yamamoto (2000), Geotail observations of the Kelvin-Helmholtz instability at the equatorial magnetotail boundary for parallel northward fields, *Journal of Geophysical Research*, *105*.

Foullon, C., C. J. Farrugia, A. N. Fazakerley, C. J. Owen, F. T. Gratton, and R. B. Torbert (2008), Evolution of Kelvin-Helmholtz activity on the dusk flank magnetopause, *Journal of Geophysical Research*, *113*, doi:10.1029/2008JA013175.

Gosling, J. T., M. F. Thomsen, S. J. Bame, and C. T. Russell (1986), Accelerated plasma flows at the near-tail magnetopause, *Journal of Geophysical Research: Space Physics*, *91*, doi:10.1029/JA091iA03p03029.

Hasegawa, H., M. Fujimoto, K. Maezawa, Y. Saito, and T. Mukai (2003), Geotail observation of the dayside outer boundary region: Interplanetary magnetic field control and dawn-dusk asymmetry, *Journal of Geophysical Research*, *108*, doi:10.1029/2002JA009667.

Hasegawa, H., M. Fujimoto, T.-D. Phan, H. Réme, A. Balogh, M. W. Dunlop, C. Hashimoto, and R. TanDokoro (2004), Transport of solar wind into Earth's magnetosphere through rolled-up Kelvin-Helmholtz vortices, *Nature*, *430*, 755–758.

Hasegawa, H., M. Fujimoto, K. Takagi, Y. Saito, T. Mukai, and H. Réme (2006), Single-spacecraft detection of rolled-up Kelvin-Helmholtz vortices at the flank magnetopause, *Journal of Geophysical Research*, *111*, doi:10.1029/2006JA011728.

Hasegawa, H., A. Retinò, A. Vaivads, Y. Khotyaintsev, M. Andre, T. K. M. Nakamura, L.-L. Teh, B. U. O. Sonnerup, S. J. Schwartz, Y. Seki, M. Fujimoto, Y. Saito, H. Reme, and P. Canu (2009), Kelvin-Helmholtz waves at the Earth's magnetopause: multiscale development and associated reconnection, *Geophysical Research Letters*, *114*, doi:10.1029/2009JA014042.

Henry, Z. W., K. Nykyri, T. W. Moore, A. P. Dimmock, and X. Ma (2017), On the dawn-dusk asymmetry of the Kelvin-Helmholtz instability between 2007 and 2013, *Journal of Geophysical Research*, *122*, 11,888–11,900, doi:10.1002/2017JA024548.

Hwang, K.-J., M. L. Goldstein, M. M. Kuznetsova, Y. Wang, A. F. Viñas, and D. G. Sibeck (2012), The first in situ observation of kelvin-helmholtz waves at high-latitude magnetopause during strongly dawnward interplanetary magnetic field conditions, *Journal of Geophysical Research: Space Physics*, *117*(A8), doi:10.1029/2011JA017256.

Johnson, J. R., C. Z. Cheng, and P. Song (2001), Signatures of mode conversion and kinetic Alfvén waves at the magnetopause, *Geophysical Research Letters*, *28*.

Kavosi, S., and J. Reader (2015), Ubiquity of Kelvin-Helmholtz waves at the Earth's magnetopause, *Nature Communications*.

King, J. H., and N. E. Papitashvili (2005), Solar wind spatial scales in and comparisons of hourly wind and ACE plasma and magnetic field data, *Journal of Geophysical Research*, *110*, doi:10.1029/2004JA010649.

Li, W., M. Andre, Y. V. Khotyaintsev, A. Vaivads, D. B. Graham, S. Toledo-Redondo, C. Norgren, P. Henri, C. Wang, B. B. Tang, B. Lavraud, Y. Vernisse, D. L. Turner, J. Burch, R. Torbet, W. Magnes, C. T. Russell, J. B. Blake, B. Mauk, B. Giles, C. Pollock, J. Fennell, A. Jaynes, L. A. Avanov, J. C. Dorellie, D. J. Gershman, W. R. Paterson, Y. Saito, and R. J. Strangeway (2016), Kinetic evidence of magnetic reconnection due to Kelvin-Helmholtz waves, *Geophysical Research Letters*, *43*, 5635–5643, doi:10.1002/2016GL069192.

Lin, D., C. Wang, W. Li, B. Tang, X. Guo, and Z. Peng (2014), Properties of Kelvin-Helmholtz waves at the magnetopause under northward interplanetary magnetic field: statistical study, *Journal of Geophysical Research: Space Physics*, *119*, 7485–7494, doi:10.1002/2014JA020379.

Ma, X., A. Otto, and P. Delamere (2014a), Interaction of magnetic reconnection and Kelvin-Helmholtz modes for large magnetic shear: 1. Kelvin-Helmholtz trigger, *Journal of Geophysical Research: Space Physics*, *119*, 781–797, doi:10.1002/2013JA019224.

Ma, X., A. Otto, and P. Delamere (2014b), Interation of magnetic reconnection and Kelvin-Helmholtz modes for large magnetic shear: 2. reconnection trigger, *Journal of Geophysical Research: Space Physics*, *119*, 808–820, doi:10.1002/2013JA019225.

Ma, X., A. Otto, P. A. Delamere, and H. Zhang (2016), Interaction between reconnection and Kelvin-Helmholtz at the high-latitude magnetopause, *Advances in Space Research*, *58*(2), 231–239.

Ma, X., P. Delamere, A. Otto, and B. Burkholder (2017), Plasma transport driven by the three-dimensional Kelvin-Helmholtz instability, *Journal of Geophysical Research: Space Physics*, *122*, 10,382–10,395, doi:10.1002/2017JA024394.

Ma, X., P. Delamere, K. Nykyri, B. Burkholder, D. Neupane, and R. Rice (2019), Comparison between fluid simulation with test particles and hybrid simulation for the Kelvin-Helmholtz instability, *Journal of Geophysical Research: Space Physics*, *124*, 6654–6668, doi:10.1029/2019JA026890.

Merkin, V. G., J. G. Lyon, and S. G. Claudepierre (2013), Kelvin-Helmholtz instability of the magnetospheric boundary in a three-dimensional global MHD simulation during northward IMF conditions, *Journal of Geophysical Research: Space Physics*, *118*, 5478–5496, doi:10.1002/jgra.50520.

Michael, A. T., K. A. Sorathia, V. G. Merkin, K. Nykyri, B. L. Burkholder, X. Ma, A. Y. Ukhorskiy, and J. Garretson (2021), Modeling Kelvin-Helmholtz Instability at the High-Latitude Boundary Layer in a Global Magnetosphere Simulation, *Geophysical Research Letters*, *48*(19), doi:10.1029/2021GL094002.

Miura, A. (1984), Anomalous transport by magnetohydrodynamic Kelvin-Helmholtz instabilities in the solar wind-magnetosphere interaction, *Journal of Geophysical Research*, *89*, 801–818.

Miura, A. (1987), Simulation of the Kelvin-Helmholtz instability at the magnetospheric boundary, *Journal of Geophysical Research*, *92*, 3195–3206.

Miura, A., and P. L. Pritchett (1982), Nonlocal stability analysis of the MHD Kelvin-Helmholtz instability in a compressible plasma, *Journal of Geophysical Research*, *87*, 7431–7444.

Moore, T. W., K. Nykyri, and A. P. Dimmock (2016), Cross-scale energy transport in space plasmas, *Nature Physics*.

Moore, T. W., K. Nykyri, and A. P. Dimmock (2017), Ion-scale wave properties and enhanced ion heating across the low-latitude boundary layer during Kelvin-Helmholtz instability, *Journal of Geophysical Research: Space Physics*, *122*, 11,128–11,153, doi:10.1002/2017JA024591.

Nykyri, K. (2013), Impact of MHD shock physics on magnetosheath asymmetry and Kelvin-Helmholtz instability, *Journal of Geophysical Reseach: Space Physics*, *118*, 5068–5081.

Nykyri, K., and A. Otto (2001), Plasma transport at the magnetopause boundary due to reconnection in Kelvin-Helmholtz vortices, *Geophysical Research Letters*, *28*, 3565–3568.

Nykyri, K., and A. Otto (2004), Influence of the Hall term on KH instability and reconnection inside KH vortices, *Annales Geophysicae*, *22*, 935–949.

Nykyri, K., A. Otto, J. Büchner, B. Nikutowski, W. Baumjohann, L. M. Kistler, and C. Mouikis (2003), Equator-S observations of boundary signatures: FTE's or Kelvin-Helmholtz waves?, in *Earth's Low-Latitude Boundary Layer*, *Geophysical Monograph*, vol. 133, edited by P. T. Newell and R. Onsager, pp. 205–210, American Geophysical Union.

Nykyri, K., A. Otto, B. Lavraud, C. Mouikis, L. M. Kistler, A. Balogh, and H. Réme (2006), Cluster observations of reconnection due to the Kelvin-Helmholtz instability at the dawnside magnetospheric flank, *Annales Geophysicae*, *24*, 2619–2643.

Nykyri, K., A. Otto, E. Adamson, and J. Mumme (2011a), Cluster observations of a cusp diamagnetic cavity: structure, size, and dynamics, *Journal of Geophysical Research*, *116*, doi:10.1029/2010JA015897.

Nykyri, K., A. Otto, E. Adamson, and A. Tjulin (2011b), On the origin of fluctuation in the cusp diamagnetic cavity, *Journal of Geophysical Research*, *116*, doi:10.1029/2010JA015888.

Nykyri, K., X. Ma, A. Dimmock, C. Foullon, A. Otto, and A. Osmane (2017), Influence of velocity fluctuations on the Kelvin-Helmholtz instability and its associated mass transport, *Journal of Geophysical Research*, *122*, 9489–9512, doi:10.1002/2017JA024374.

Nykyri, K., X. Ma, B. Burkholder, R. Rice, J. R. Johnson, E.-K. Kim, P. Delamere, A. Michael, K. Sorathia, D. Lin, S. Merkin, S. Fuselier, J. Broll, O. Le Contel, D. Gershman, I. Cohen, B. Giles, R. J. Strangeway, C. T. Russell, and J. L. Burch (2021), MMS observations of the multiscale wave structures and parallel electron heating in the vicinity of the southern exterior cusp, *Journal of Geophysical Research: Space Physics*, *126*(3), doi:10.1029/2019JA027698.

Otto, A. (1990), 3D resistive MHD computations of magnetospheric physics, *Computer Physics Communications*, *59*, 185–195.

Otto, A., and D. H. Fairfield (2000), Kelvin-Helmholtz instability at the magnetotail boundary: MHD simulation and comparison with Geotail observations, *Journal of Geophysical Research*, *105*, 21,175–21,190.

Paschmann, G., B. U. Ö. Sonnerup, I. Papamastorakis, G. Haerendel, S. J. Bame, J. R. Asbridge, J. T. Gosling, C. T. Russell, and R. C. Elphric (1979), Plasma acceleration at the Earth's magnetopause: evidence for reconnection, *Nature*, *282*, 243–246.

Pollock, C., T. Moore, A. Jacques, J. Burch, U. Gliese, Y. Saito, T. Omoto, L. Avanov, A. Barrie, V. Coffey, J. Dorelli, D. Gershman, B. Giles, T. Rosnack, C. Salo, S. Yokota, M. Adrian, C. Aoustin, C. Auletti, S. Aung, V. Bigio, N. Cao, M. Chandler, D. Chornay, K. Christian, G. Clark, G. Collinson, T. Corris, A. D. L. Santos, R. Devlin, T. Diaz, T. Dickerson, C. Dickson, A. Diekmann, F. Diggs, C. Duncan, A. Figueroa-Vinas, C. Firman, M. Freeman, N. Galassi, K. Garcia, G. Goodhart, D. Guererro, J. Hageman, J. Hanley, E. Hemminger, M. Holland, M. Hutchins, T. James, W. Jones, S. Kreisler, J. Kujawaski, V. Lavu, J. Lobell, E. LeCompte, A. Lukemire, E. MacDonald, A. Mariano, T. Mukai, K. Narayanan, Q. Nguyan, M. Onizuka, W. Paterson, S. Persyn, B. Piepgrass, F. Cheey, A. Rager, T. Raghuram, A. Ramil, L. Reichenthal, H. Rodriguez, J. Rouzaud, A. Rucker, Y. Saito, M. Samara, J.-A. Sauvaud, D. Schuster, M. Shappirio, K. Shelton, D. Sher, D. Smith, K. Smith, S. Smith, D. Steinfeld,

R. Szymkiewicz, K. Tanimoto, J. Taylor, C. Tucker, K. Tull, A. Uhl, J. Vloet, P. Walpole, S. Weidner, D. White, G. Winkert, P.-S. Yeh, and M. Zeuch (2016), Fast plasma investigation for Magnetospheric Multiscale, *Space Science Reviews*, *199*, 331–406, doi:10.1007/s11214-016-0245-4.

Potter, D. (1973), *Computational Physics*, John Wiley and Sons.

Russell, C. T., B. J. Anderson, W. Baumjohann, K. R. Bromund, D. Dearborn, D. Fischer, G. Le, H. K. Leinweber, D. Lenema, W. Magnes, J. D. Means, M. B. Moldwin, R. Nakamura, D. Pierce, F. Plaschke, K. M. Rowe, J. A. Slavin, R. J. Strangeway, R. Torbet, C. Hagen, I. Jernej, A. Valavanoglou, and I. Ricter (2016), The Magnetospheric Multiscale magnetometers, *Space Science Reviews*, *199*, 189–256, doi:10.1007/s11214-014-0057-3.

Sonnerup, B. U. Ö., and M. Scheible (1998), *Analysis Methods for Multi-Spacecraft Data*, chap. Minimum and Maximum Variance Analysis, pp. 185–220, International Space Science Institute.

Sonnerup, B. U. Ö., G. Paschmann, I. Papamastorakis, N. Sckopke, G. Haerendel, S. J. Bame, J. R. Asbridge, J. T. Gosling, and C. T. Russell (1981), Evidence for magnetic field reconnection at the Earth's magnetopause, *Journal of Geophysical Research: Space Physics*, *86*, doi:10.1029/JA086iA12p10049.

Sorathia, K. A., V. G. Merkin, A. Y. Ukhorskiy, R. C. Allen, K. Nykyri, and S. Wing (2019), Solar wind ion entry into the magnetosphere during northward IMF, *Journal of Geophysical Research: Space Physics*, *124*, doi: doi.org/10.1029/2019JA026728.

Stawarz, J. E., S. Eriksson, F. D. Wilder, R. E. Ergun, S. J. Schwartz, A. Pouquet, J. L. Burch, B. L. Giles, Y. Khotyaintsev, O. L. Contel, P.-A. Lindqvist, W. Magnes, C. J. Pollock, C. T. Russll, R. J. Strangeway, R. B. Torbert, L. A. Avanov, J. C. Dorelli, J. P. Eastwood, D. J. Gershman, K. A. Goodrich, D. M. Malaspina, G. T. Marklund, L. Mirioni, and A. P. Sturner (2016), Observations of turbulence in a Kelvin-Helmholtz event on 8 September 2015 by the Magnetospheric Multiscale mission, *Journal of Geophysical Research*, *121*, 11,021–11,034, doi:10.1002/10JA023458.

Taylor, M. G. G. T., B. Lavraud, C. P. Escoubet, S. E. Milan, K. Nykyri, M. W. Dunlop, J. A. Davies, R. H. W. Friedel, H. Frey, Y. V. Bogdanova, A. Asnes, H. Laasko, P. Trvincek, A. Masson, H. Opgenoorth, C. Vallat, A. N. Fazakerley, A. D. Lahiff, C. J. Owen, F. Pitout, Z. Pu, C. Shen, Q. G. Zong, H. Rme, J. Scudder, and T. L. Zhang (2008), The plasma sheet and boundary layers under northward IMF: a multi-point and multi-instrument perspective, *Advances in Space Research*, *41*, 1619–1629.

Taylor, M. G. G. T., H. Hasegawa, B. Lavraud, T. Phan, C. P. Escobet, M. W. Dunlop, Y. V. Bogdanova, A. L. Borg, M. Volwerk, J. Berchem, O. D. Constantinescu, J. P. Eastwood, A. Masson, H. Laakso, J. Soucek, A. N. Fazakerley, H. Frey, E. V. Panov, C. Shen, J. K. Shi, D. G. Sibeck, Z. Y. Pu, J. Wang, and J. A. Wild (2012), Spatial distribution of rolled up Kelvin-Helmholtz vortices at Earth's dayside and flank magnetopause, *Annales Geophysicae*, *30*, 1025–1035, doi:10.5194/angeo-30-1025-2012.

Torbert, R. B., C. T. Russell, w. Magnes, R. E. Ergun, P.-A. Lindqvist, O. LeContel, H. Vaith, J. Macri, S. Myers, D. Rau, J. Needell, B. King, M. Granoff, M. Chutter, I. Dors, G. Olsson, Y. V. Khotyaintsev, A. Eriksson, C. A. Kletzing, S. Bounds, B. Anderson, W. Baumjohann, M. Steller, K. Bromund, G. Le, R. Nakamura, R. J. Strangeway, H. K. Leinweber, S. Tucker, J. Westfell, D. Fisher, F. Plaschke, J. Porter, and K. Lappalainen (2016), The FIELDS instrument suite on MMS: scientific objectives, measurements, and data products, *Space Science Reviews*, *199*, 105–135, doi:10.1007/s11214=014-0109-8.

Wilder, F. D., R. E. Ergun, S. J. Schwartz, D. L. Newman, S. Eriksson, J. E. Stawarz, M. V. Goldman, K. A. Goodrich, D. J. Gershman, D. M. Malaspina, J. C. Holmes, A. P. Sturner, J. L. Burch, R. B. Torbert, P.-A. Lindqvist, G. T. Marklund, Y. Khotyaintsev, R. J. Strangeway, C. T. Russel, C. J. Pollock, B. L. Giles, J. C. Dorelli, L. A. Avanov, W. R. Patterson, F. Plaschke, and W. Magnes (2016), Observations of large-amplitude, parallel, electrostatic waves associated with the Kelvin-Helmholtz instability by the Magnetospheric Multiscale mission, *Geophysical Research Letters*, *43*, 8859–8866, doi:10.1002/2016GL070404.

Wing, S., J. R. Johnson, P. T. Newell, and C.-I. Meng (2005), Dawn-dusk asymmetries, ion spectra, and sources in the northward interplanetary magnetic field plasma sheet, *Journal of Geophysical Research*, *110*, doi:10.1029//2005JA011086.

Zhao, C., C. T. Russell, R. J. Strangeway, S. M. Petrinec, W. R. Paterson, M. Zhou, B. J. Anderson, W. Baumjohann, K. R. Bromund, M. Chutter, D. Fischer, G. Le, R. Nakamura, F. Plaschke, J. A. Slavin, R. B. Torbert, and H. Y. Wei

(2016), Force balance at the magnetopause determined with MMS: application to flux transfer events, *Geophysical Research Letters*, *43*, 11,941–11,947, doi: 10.1002/2016GL071568.

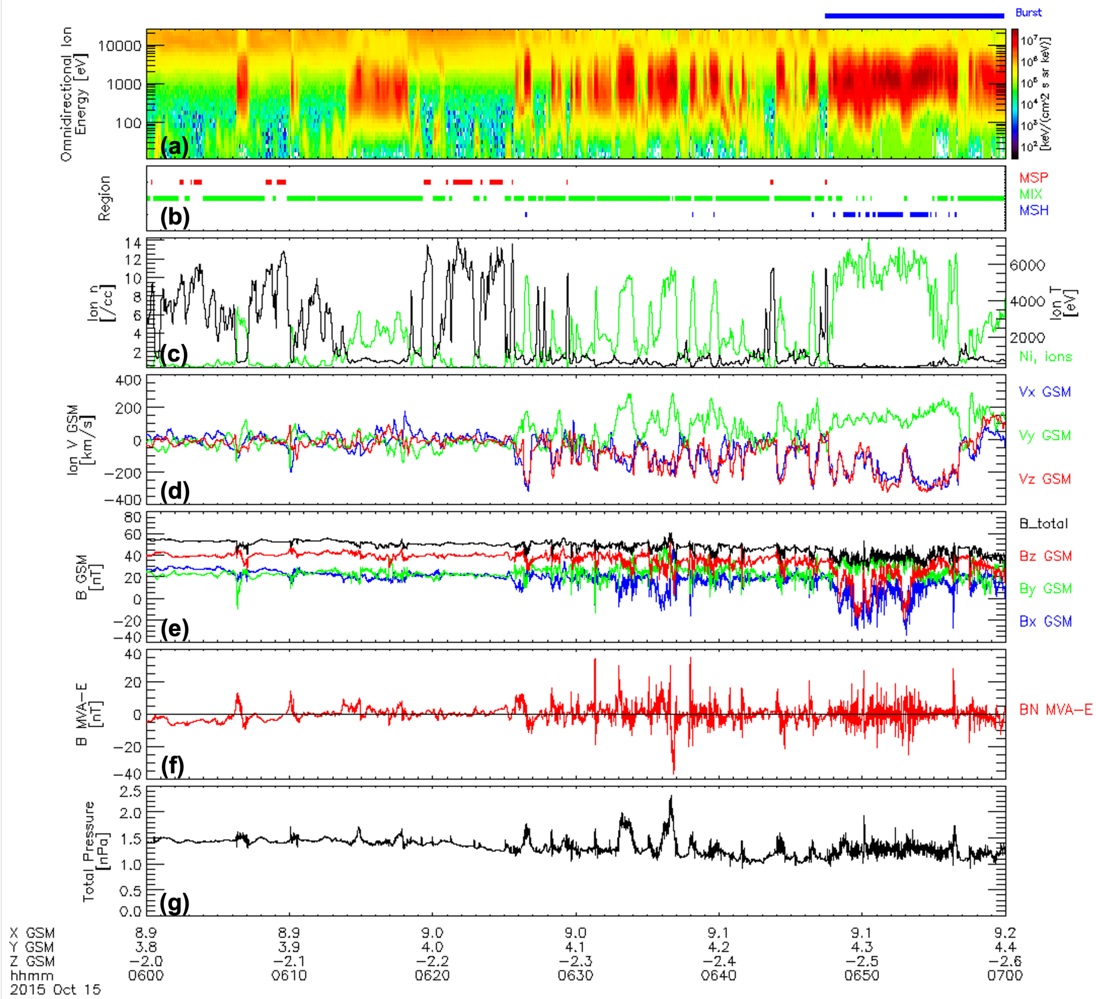

Figure 1. MMS observations of (a) omnidirectional ion energies; (b) plasma region; (c) ion density (green) and temperature (black); (d) ion bulk velocity in GSM coordinates; (e) direct current magnetic field in GSM coordinates; (f) the normal component of the magnetic field; and (g) total pressure from 06:00 to 07:00 UT on 15 October 2015. Ion data is taken from the Fast Plasma Investigation (FPI) and magnetic field data is from the Flux Gate Magnetometer (FGM) aboard MMS1. Burst mode data is available for the intervals marked in blue above the panels.

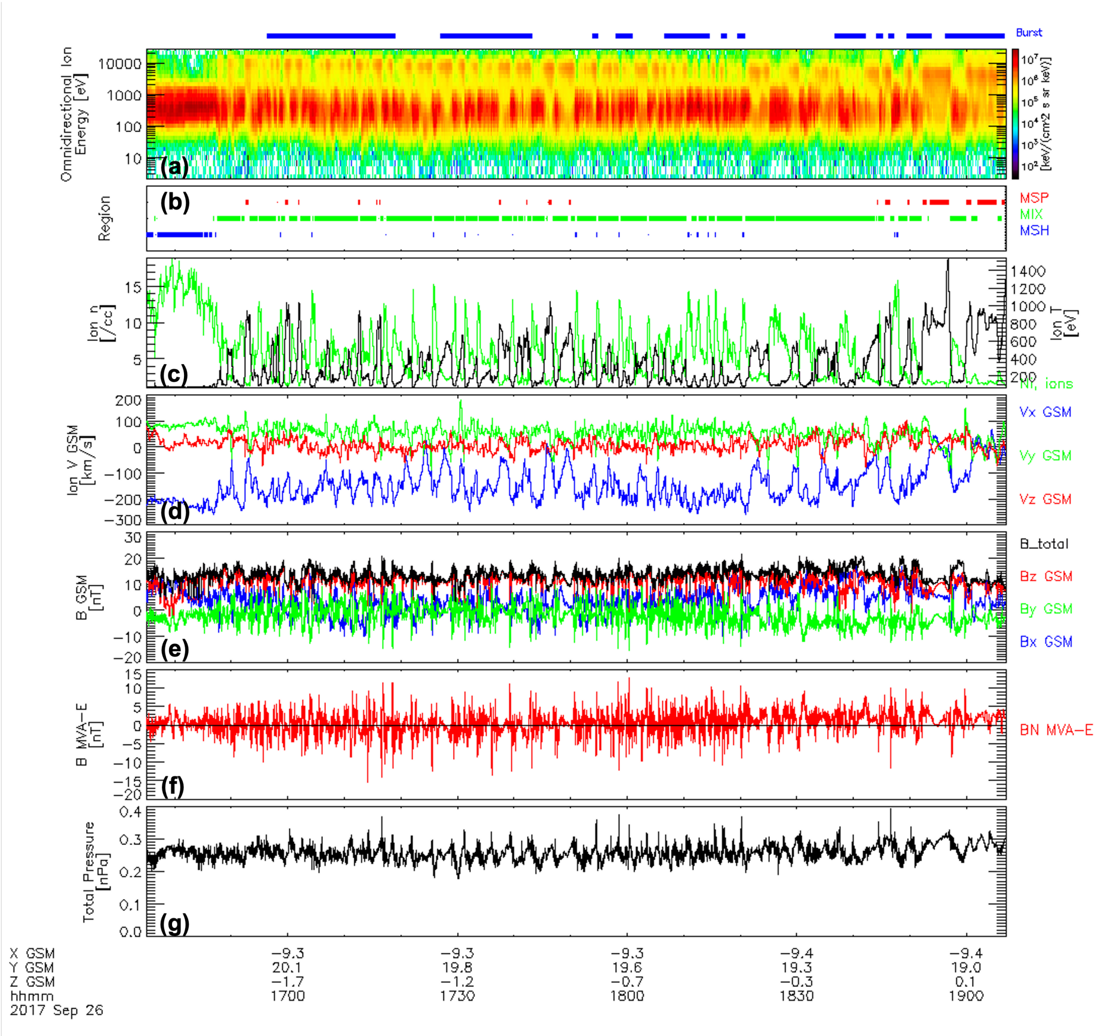

228 **Figure 2.** MMS observations as in Figure 1 from 16:35 to 19:07 UT on 26 September 2017.
229 Ion data is taken from the Fast Plasma Investigation (FPI) and magnetic field data is from the
230 Flux Gate Magnetometer (FGM) aboard MMS1. Burst mode data is available for the intervals
231 marked in blue at top.

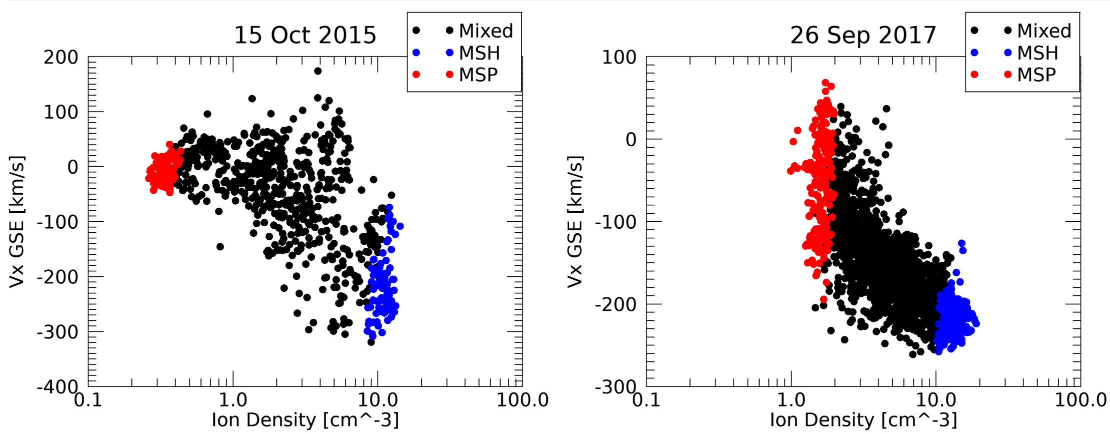

Figure 3. MMS observations of tailward ion velocity as a function of ion density for 06:00-07:00 on 15 October 2015 (left) and 16:35-19:07 on 26 September 2017. Blue (red) points were identified as magnetosheath (magntospheric) plasma. Mixed and ambiguous regions are plotted in black. For the 2017 example event, ions show clear evidence of roll-over within the KHI vortex, low density plasma typically associated with the magnetosphere is moving tailward with the faster magnetosheath plasma, but this is not seen for the 2015 example event. The overall shape of both events however, is consistent with previous studies of the KHI.

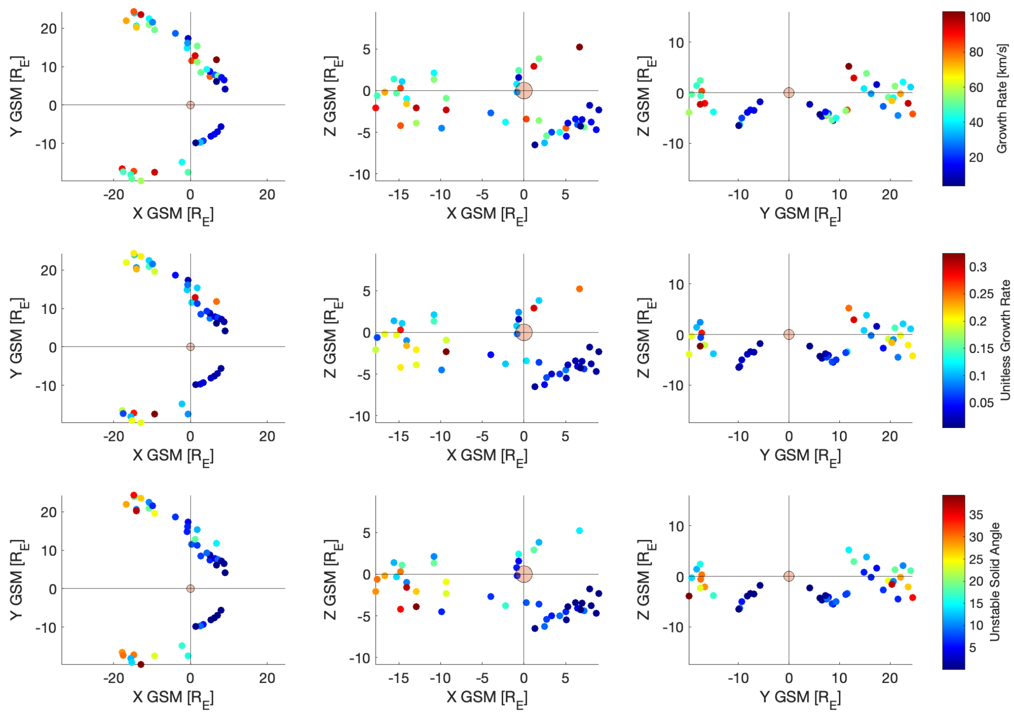

Figure 4. Growth rates (GR, top row), unitless growth rates (UGR, middle row), and unstable solid angles (USA, bottom row) plotted with respect to the KHI's location along the magnetopause in GSM X-Y plane (left column), X-Z plane (middle column), and Y-Z plane (right column).

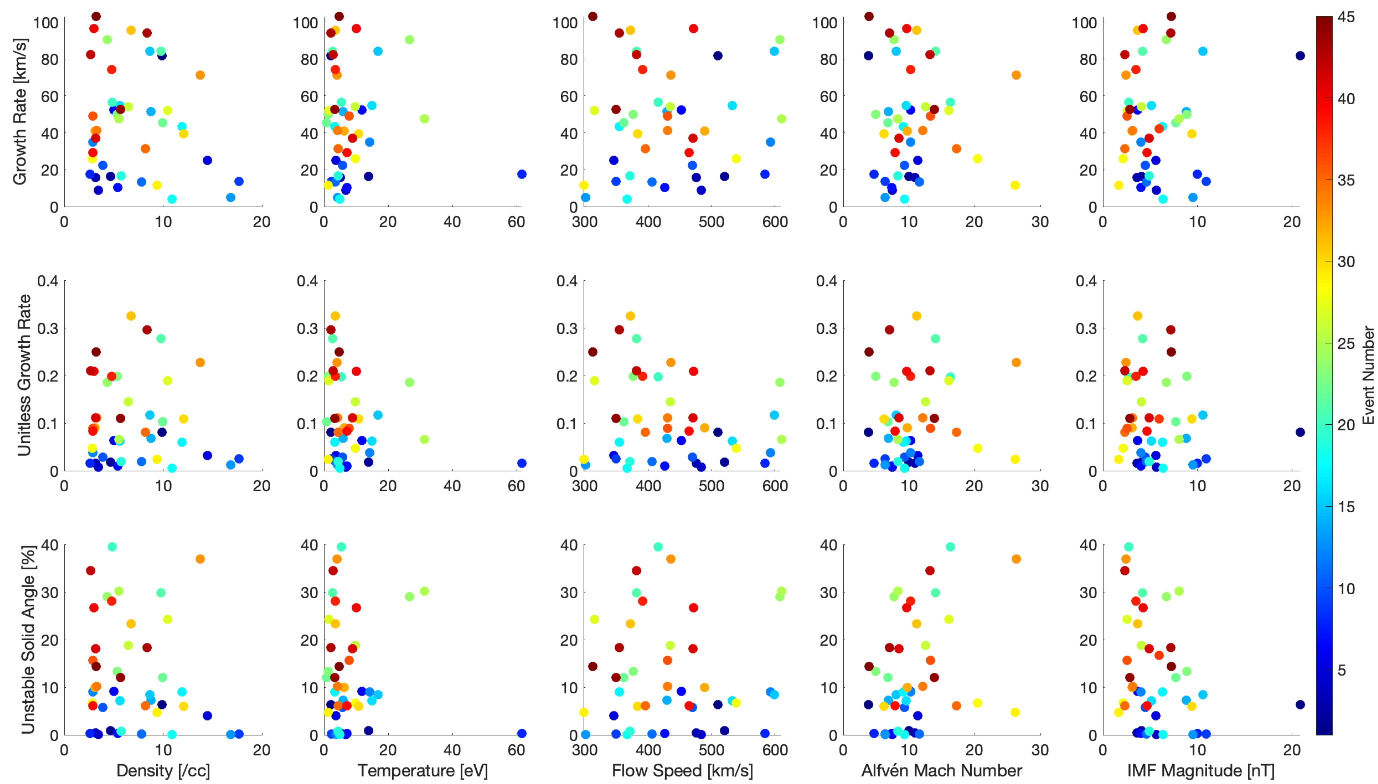

Figure 5. KHI growth rates (GR, top), unitless growth rates (UGR, middle), and unstable solid angles (USA, bottom) as a function of SW density (far left), temperature (center left), flow speed (center), Alfvén mach number (center right), and average IMF magnitude (far right). Other than a selection window from 295-610 km/s flow speed, GR, UGR, and USA are independent of solar wind parameters. The color bar indicates each unique event for comparison from plot to plot.

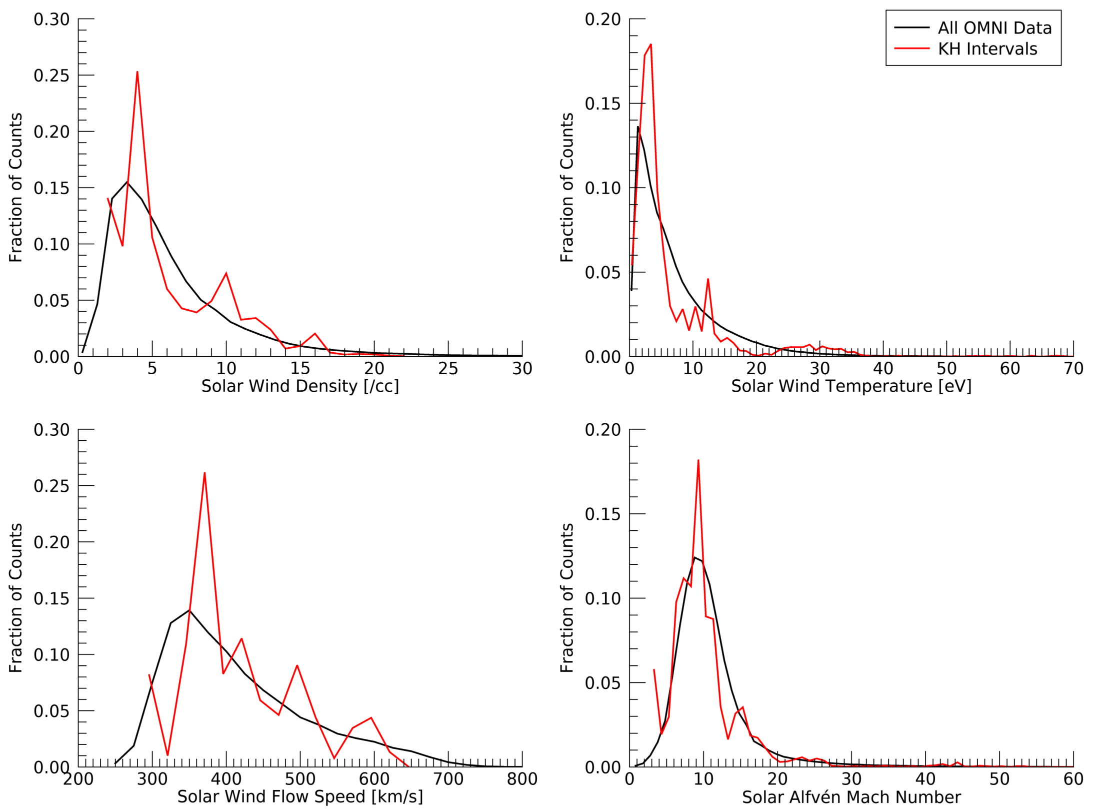

Figure 6. Normalized histograms of solar wind density (top left), temperature (top right), speed (bottom left), and Alfvén Mach number (bottom right) for the complete time range considered in this study, 01 September 2015 to 31 March 2020 (black), and for the intervals during which MMS observed the KHI (red).

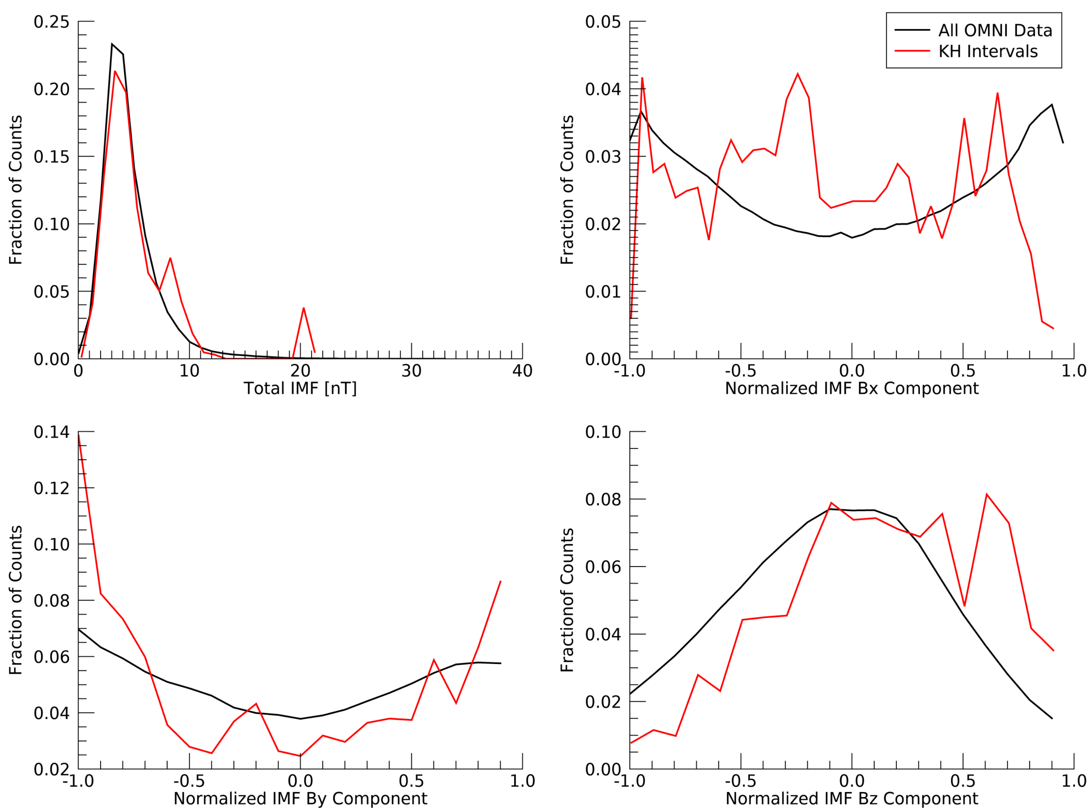

Figure 7. Normalized histograms of IMF magnitude (top left) and normalized IMF components for the complete time range considered in this study, 01 September 2015 to 31 March 2020 (black), and for the intervals during which MMS observed the KHI (red).

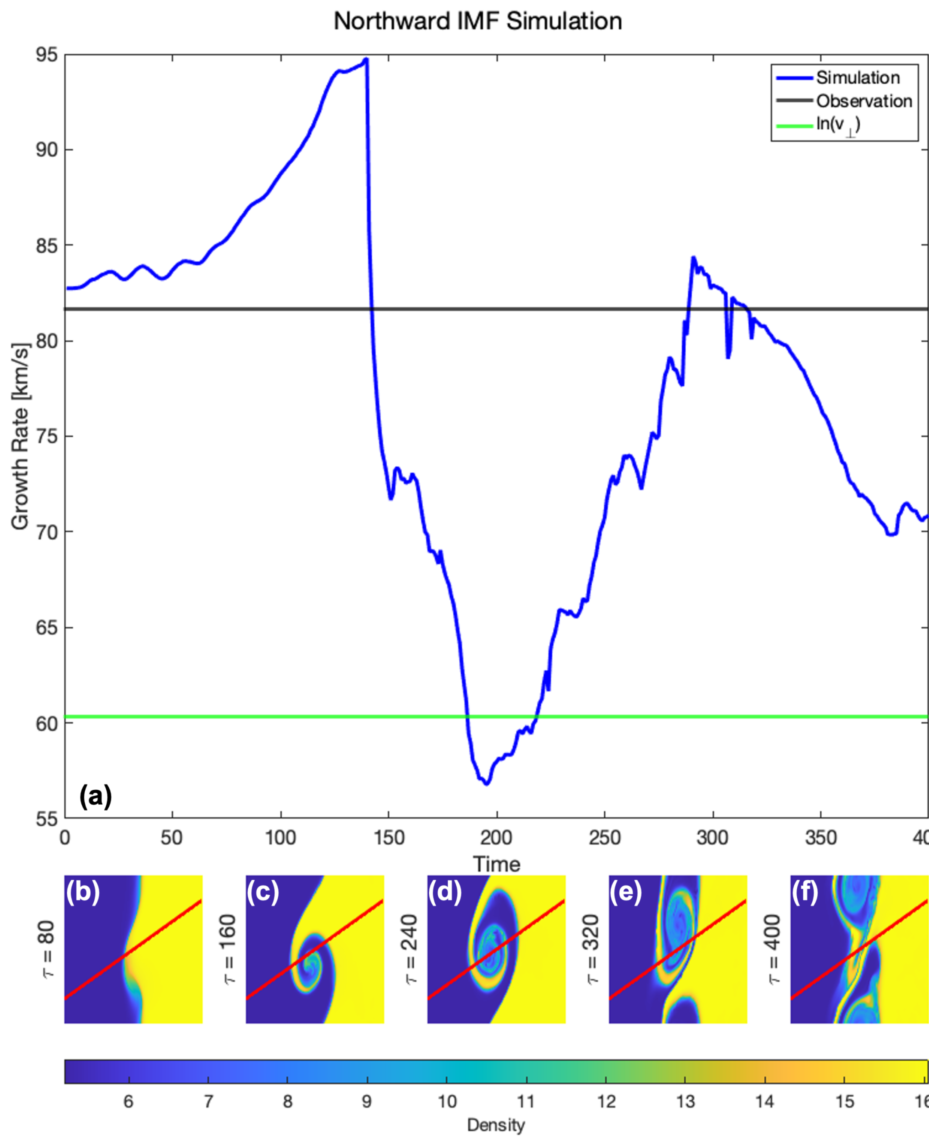

Figure 8. Growth rates were calculated and plotted as a function of time (a) using data from 2D MHD simulations of a dusk flank KHI occurring during Northward IMF. Initial conditions of the simulation are based on the event MMS observed on 08 September 2015. Density data from several time steps within the simulation (b)-(f) show the development of the KHI. Cuts, as indicated by the red line in panels (b)-(f), were taken through the instability at every simulation time step. The black line (a) indicates the growth rate for the MMS event on which the simulation is based. The green line (a) indicates the theoretical growth rate for the simulation as determined by the slope of the linear portion of $\ln(v_\perp)$ plotted as a function of time.

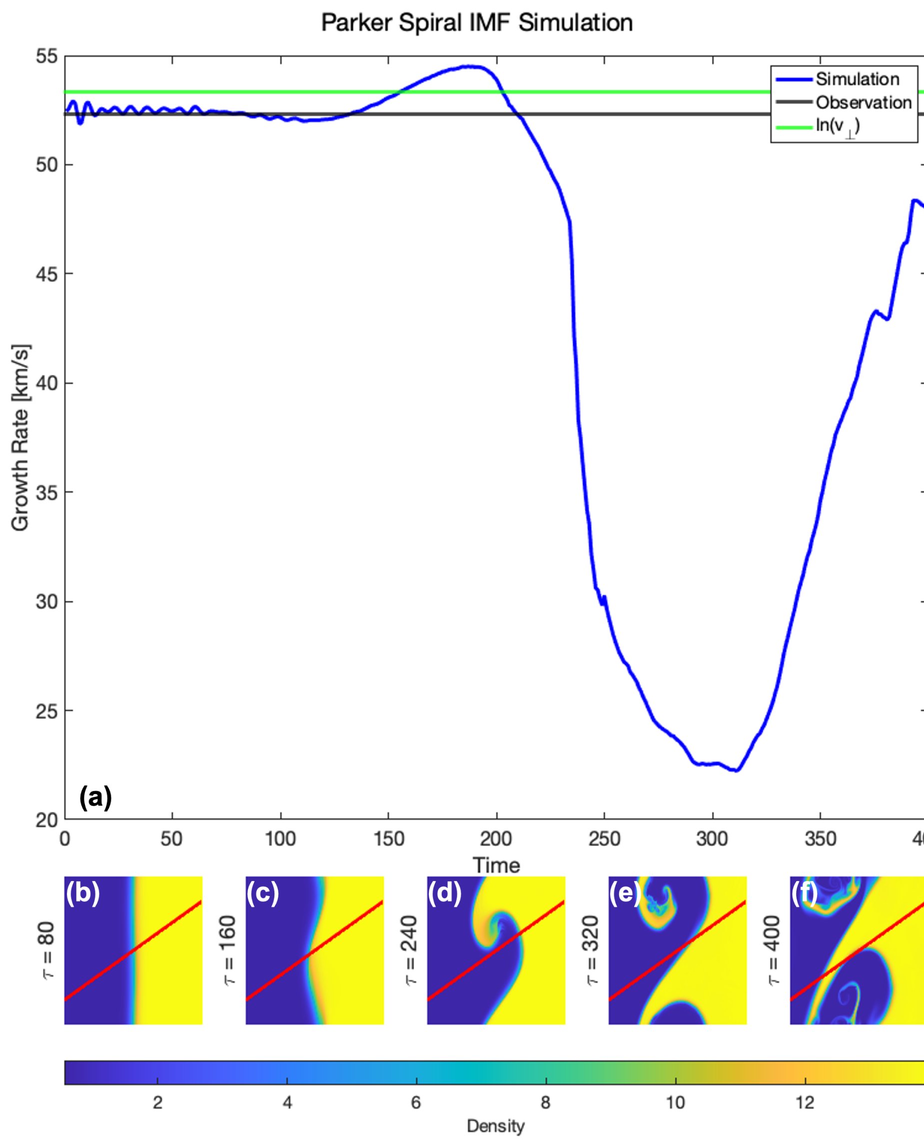

Figure 9. The KHI growth rates as in Figure 8 for a 2D MHD simulation of a dusk flank KHI occurring during Parker Spiral IMF orientation. Initial conditions of the simulation are based on the event MMS observed on 18 October 2015.

Supporting Information for
"Characteristics of Kelvin-Helmholtz Waves as Observed by the MMS from September 2015 to March 2020"

Rachel Rice[1], Katariina Nykyri[1], Xuanye Ma[1], Brandon Burkholder[2]

[1]Embry-Riddle Aeronautical University, Department of Physical Sciences, Center for Space and Atmospheric Research

[2]University of Maryland Baltimore County, Goddard Planetary Heliophysics Institute

Contents

Additional Supporting Information (Files uploaded separately)

1. Captions for large Tables 1 and 2

Automated Region Sorting

The magnetosheath is characterized by cold, dense plasma flowing tailward with the shocked solar wind. The magnetosphere, on the other hand, is comprised of hot, tenuous plasma which is relatively stagnant. Thus, we have 3 plasma parameters, density, temperature, and tailward velocity, which may be used to easily and automatically distinguish the magnetosheath and magnetopause. Due to the mixing and heating which occurs within the KH vortex, and the possibility of reconnection dragging less dense magnetosphere tailward with sheath-like speeds, no one parameter will be sufficient to separate the regions. Instead, we look for a combination of two or three parameters which will allow for the automated identification of the magnetosheath and magnetosphere. Table 1 lists all of the parameters we considered and their relative values in each region.

Corresponding author: Rachel Rice, `ricer4@my.erau.edu`

Condsider a ratio of density and temperature, n/T. In the cold, dense magnetosheath, n/T is large. In the hot, tenuous magnetosheath, n/T is small.

In the magnetosheath the GSM$-X$ component of velocity is typically large and negative, flowing with the shocked solar wind. The GSM$-X$ component of velocity is typically small, either positive or negative, in the magnetosphere. For simplicity we define the tailward velocity such that it is strictly positive, $v_{tail} = |v_X - \max v_x|$. The product of density and tailward velocity, nv_{tail} is large in the magnetosheath and small in the magnetosphere.

We may combine the previous two parameters in to a single ratio, nv_{tail}/T. This is large in the magnetosheath and small in the magnetosphere.

Next consider specific entropy, $S = T/n^{2/3}$. In the cold dense magnetosheath S is small. In the hot, tenuous magnetosphere, S is large.

Recalling our definition of tailward velocity, we may also consider ratios of the specific entropy and tailward velocity, S/v_{tail} and v_{tail}/S. In the sheath, S/v_{tail} is small, and it is large in the magnetosphere. In the magnetosheath v_{tail}/S is large, and in the magnetosphere it is small.

When using the above parameters, we first determined a mean magnetopause value for each event. Then created cutoff values for each region based on the magnetopause value. Mean values of density and temperature in each isolated region were compared with typical values for the magnetosheath and magnetosphere. Mean values of density, velocity, and magnetic field were also used to calculate growth rates (GR), unitless growth rates (UGR), and unstable solid angles (USA).

In order to determine the magnetopause value, we first sort a given parameter in ascending order. A percentage of the largest and smallest values are collected, and the mean of these extreme values is labeled the magnetopause value, mp. We use a subset, rather than all, of the data for a given event, to avoid any effects from the spacecraft spending more time in one region than the other.

The percentage of data used to determine mp was varied from including the largest and smallest 2.5% (5% total) of all data to including the largest and smallest 25% (50% total) of all available data points. Once mp is determined, we can then use it to set cutoff values defining the magnetosheath and magnetosphere.

In the region in which a given parameter is expected to be large, cutoff values were varied from $1.0 * mp$ to $1.9 * mp$. The most restrictive cutoff values ($> 1.7 * mp$) were ruled out because they did not return a reasonable number of data points in both regions. Fore some events, no MMS observations fit the more restrictive criteria. The more relaxed cutoffs ($< 1.3*mp$), included too much mixed plasma from regions already strongly affected by the KHI. The inclusion of such mixed plasma had a significant but unpredictable effect on the final results. Marginal cutoff values from $1.4*mp$ to $1.6*mp$ all produce comparable results. Within this range of cutoff values, density and temperature show only small variations and match well with expected values for both the real spacecraft and simulated data.

In the region in which a given parameter is expected to be small, cutoff values were varied from $0.1 * mp$ to $1.0 * mp$. The more relaxed cutoffs ($> 0.7 * mp$) included too much plasma already affected by mixing and heating processes in the KHI. The most restrictive cutoff values ($< 0.3*mp$) are too restrictive, yielding little to no plasma in the region. The marginal cutoff values ($0.4*mp$ to $0.6*mp$), again seem to be the best choice. However, the mean density and temperature of the regions identified using these cutoffs were not reasonable for any of our tested parameters. A check against simulation data also showed poor agreement with the known values. Thus, no parameter performed well to identify the region in which it is expected to be small.

The percentage of data used to determine mp and the cutoff values were varied in parallel. Plots of the density and temperature for each identified region were created for all combinations of mp and cutoff values. Figure 1 shows an example of these plots for the magnetosheath density of the KHI encounter on 15 October 2015. The parameters which are expected to be large in the sheath (n/T, nv_{tail}, nv_{tail}/T, and v_{tail}/S), return density values from ≈ 9 to 12 /cc, in line with expectations for the sheath. Parameters which are small in the magnetosheath (S and S/v_{tail}) return density values less than 6 /cc, which is lower than expected for the typical sheath.

Likewise Figure 2 shows an example of these plots for the magnetosphere density of the KHI encounter on 15 October 2015. The parameters which are expected to be large in the magnetosphere (S and S/v_{tail}), return density values ≈ 0.5 /cc, in line with expectations for the magnetosphere. Parameters which are small in the magnetosheath (n/T,

nv_{tail}, nv_{tail}/T, and v_{tail}/S) return density values between 1 and 2 /cc, which is higher than expected for the typical magnetopshere.

We found of the percent of data used to determine the magnetopause value has only a small affect on the mean values of density (as can be seen in Figures 1 and 2) and temperature of each region and on the final calculations of GR, UGR, and USA. As such, we chose to use the smallest and largest 12.5% (25% total) of all data for a given parameter when determining the magnetopause value. This ensures we are not only considering outliers (as would be the case using too little data), but should not be strongly effected if the spacecraft spends more time on one side of the boundary than the other (as would happen if we used all available data).

Because no parameter performed well for the region in which it is expected to be small, we must use two separate parameters: one large in the magnetosheath and one large in the magnetosphere. We chose nv_{tail}/T as our sheath parameter and S as our magnetosphere parameter. Both of these parameters produce consistent results over the range of marginal cutoff values ($1.4 * mp$ to $1.6 * mp$), suggesting they are robust and not overly sensitive to the selection of our cutoff value. Thus, in order to balance the desire to select the most pure plasma from each region and the need to have a meaningful number of data points in each region, we settled on the cutoff value $1.5 * mp$.

Once selected, the parameters and cutoff values were also tested on simulation data. Both nv_{tail}/T and S performed well, isolating regions in which plasma parameters agreed well with the known values. This can be seen in Figure 3, where the density as determined by our method is plotted in blue for the duration of the simulations, and the known initial value is marked in black. The density of the regions isolated with these parameters is within 0.15/cc of the initial value for the duration of the NIMF simulation, and within 0.3/cc of the initial value for the duration of the PSIMF simulation, which indicates our methodology will work well even for the late stage KHI with significant mixing.

Our new methodology was also compared with a region sorting technique previously published in *Moore et al.* [2017]. In that study, histograms of the most common energy channel in each time step are used to determine the typical energy value of the magnetosheath and magnetosphere. The log mean average of energy in both regions is considered representative of the mixed plasma region. Each time step is sorted into the region to which its weighted mean energy is closest. For KHI where the magnetosheath and magnetospheric energies are well separated, this method works well and produces similar results as the new method presented here, as can be see in Figure 4 for the example events used in the main text. In all cases, the new method sorts more plasma into the mixed region than the Moore method, which we prefer as the resulting regions are more representative of the "pure" magnetosheath and magnetosphere.

We use the KHI event observed on 26 September 2017, shown in Figure 5, as an example of the selection of only pure magnetosheath. Plots of the MMS orbit show it skimming the the magnetopause boundary primarily on the magnetosphere side with only a brief excursion to the magnetosheath. Solar wind density is ≈ 8 /cc, yielding a pure magnetosheath density of $\approx$ 32 /cc according to MHD shock physics. MMS observes such high density only at the very end of the interval, suggesting that MMS observes pure sheath only at the end of the interval and is otherwise in mixed and magnetospheric plasma. As can be seen in Figure 6, the new method identifies only the portion of the MMS observations where density is nearly 30 /cc as pure sheath. The Moore method selects an early portion of the data as magnetosheath plasma based on its energy, but the density and temperature are more consistent with mixed plasma. This is preferable in our work, as our goal is to calculate GR, UGR, and USA using data from only pure magnetosheath and magnetosphere plasma.

In both simulations and real MMS data, it is important to remember the growth rate is dependent upon the path of the satellite through the instability (or the geometry of the cut in simulation space). Figure 7 demonstrates the effect of cut geometry on growth rate for both the NIMF and PSIMF simulations. Simulation data was recorded along four cut geometries as shown in the bottom panels of Figure 7. One cut is perpendicular to the boundary (black), one is parallel to the boundary on the magnetosheath side (cyan), another is parallel to the boundary on the magnetosphere side (magenta), and the final cut is between perpendicular and parallel to the boundary (red). Data from each cut was used to calculate the KHI growth rate at every time step as shown in the top panels of Figure 7 (colors in the growth rate plot correspond with each cut). The perpendicular and intermediate cuts are able to capture pure plasma on either side of the boundary at all time steps, and produce similar results which match well with the observational values from the real events on which they are based. The parallel cuts do not capture both regions of plasma until the KHI is well developed, and as such produce much lower growth rates until later in the simulations.

Our method of separating the regions requires the satellite observes both the magnetosheath and magnetosphere, and works best when the regions are observed for roughly equal times. We can use our method to separate the regions in skimming cuts which observe much more of one region than the other, but such cuts are likely to underestimate the growth rate.

Figures 1 to 7

Tables 1 and 2

Table 1. Tested parameters and the relative values in the magnetosheath and magnetosphere.

Parameter	Magnetosheath	Magnetosphere
n/T	large	small
nv_{tail}	large	small
nv_{tail}/T	large	small
S	small	large
S/v_{tail}	small	large
v_{tail}/S	large	small

Table 2. Normalization constants for the 2D MHD simulations.

Quantity	Northward	Parker spiral
Magnetic field B_0 (nT)	71.5	30.23
Number Density n_0 (/cc)	12.36	2.78
Length scale L_0 (km)	640	640
Velocity V_A (km/s)	443	395.21
Time t_0 (s)	1.35	1.62

Caption for Long Table 1

MMS observed 45 KHI from September 2015 to March 2020. Onset IMF orientation and magnitude, average IMF orientation and magnitude, solar wind flow speed, Alfvén Mach number, temperature, and density are determined using 1 minute OMNI data, which is available for 44 of the 45 events. Here, "onset" refers to the time at which KHI first observes the KHI, as we cannot predict how long the KHI may have been operating before MMS observes it. The OMNI data we report is convected to the bow shock nose, but not to the KHI observation point. Additional transit times to the observation point is estimated using the magnetosheath velocity, are typically small, and have little to no effect on the observed SW conditions.

Caption for Long Table 2

Boundary normal directions were determined using the maximum variance of the convective electric field (MVA-E) technique. The outward pointing normal for a stationary boundary is the direction of maximum variance in the $\mathbf{v}\times\mathbf{B}$ electric field. The Minimum Faraday Residue (MFR) method determines the normal direction and velocity of a moving boundary. The normal direction is well determined when the maximum eigenvalue of the variance matrix is significantly larger than the intermediate eigenvalue for MVA-E, yielding an eigenvalue ratio of 5 or greater. Likewise, the MFR normal direction is well determined when the intermediate eigenvalue of the residue matrix is significantly larger than the minimum eigenvalue. In all cases, the velocity of the boundary is small, as is expected for events in which the velocity is primarily tangential to the boundary, like the KHI. MVA-E and MFR thus produce similar normal directions, but MVA-E has larger eigenvalue ratios. For this reason, we use MVA-E in our analysis.

References

Moore, T. W., K. Nykyri, and A. P. Dimmock (2017), Ion-scale wave properties and enhanced ion heating across the low-latitude boundary layer during Kelvin-Helmholtz instability, *Journal of Geophysical Research: Space Physics*, *122*, 11,128–11,153, doi:10.1002/2017JA024591.

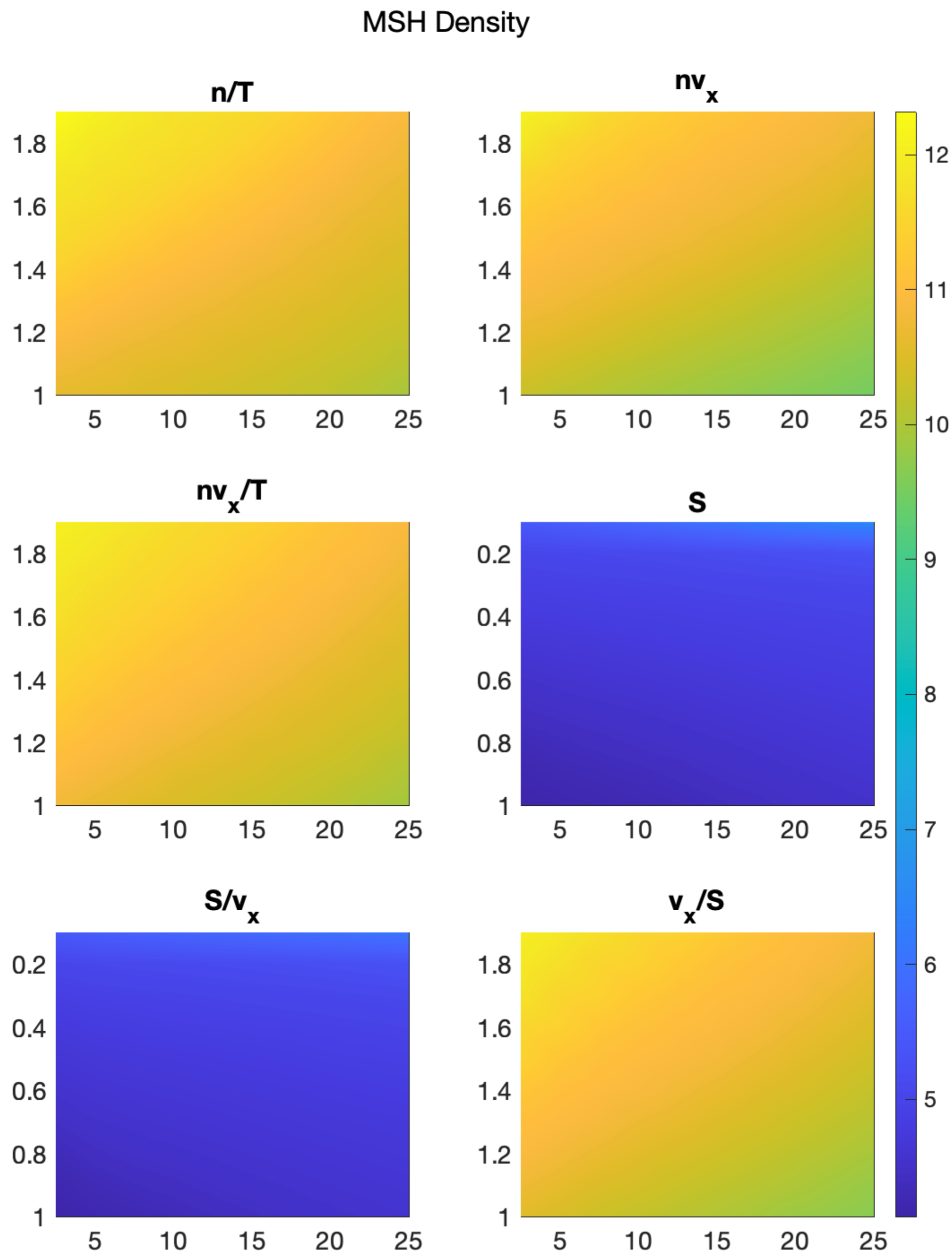

Figure 1. Magnetosheath density for all parameters and combinations of magnetopause values and cutoff values. The percent of data used to determine the magnetopause value increases from right to left on the X-axis. Cutoff values become more restrictive from bottom to top along the Y-axis. The parameters which are large in the sheath (n/T, nv_{tail}, nv_{tail}/T, and v_{tail}/S) return more reasonable values than the parameters which are small in the sheath (S and S/v_{tail}).

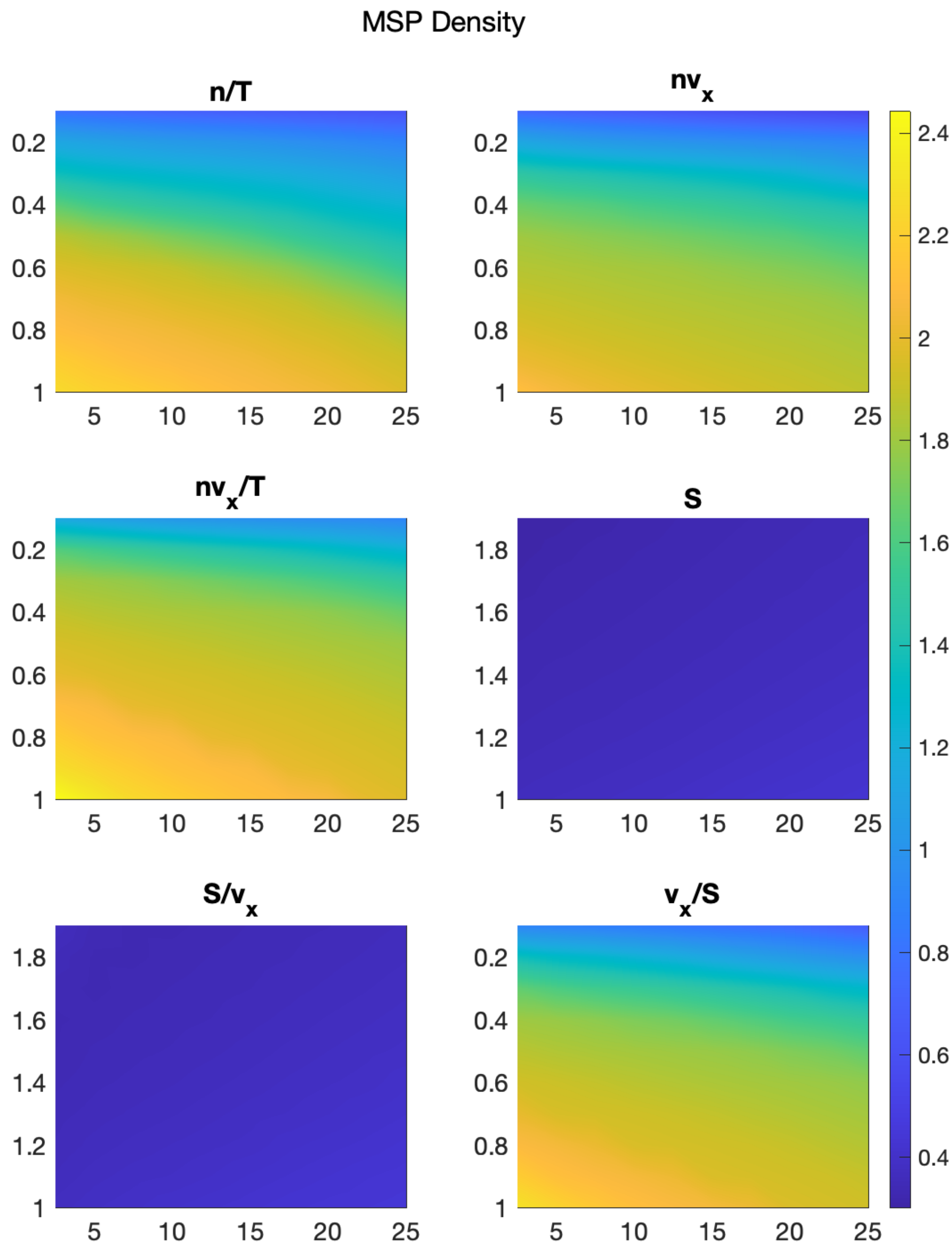

Figure 2. Magnetosphere density for all parameters and combinations of magnetopause values and cutoff values. The percent of data used to determine the magnetopause value increases from right to left on the X-axis. Cutoff values become more restrictive from bottom to top along the Y-axis. The parameters which are large in the sheath (S and S/v_{tail}) return more reasonable values than the parameters which are small in the sheath (n/T, nv_{tail}, nv_{tail}/T, and v_{tail}/S).

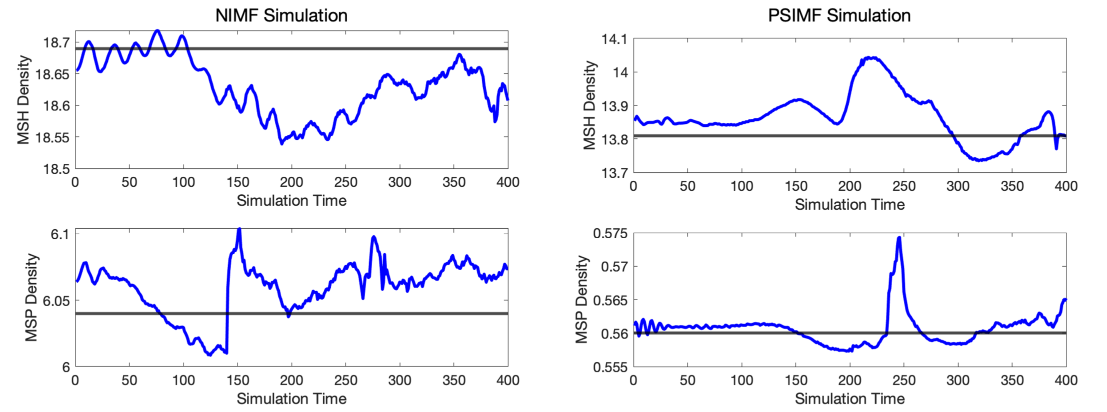

Figure 3. Magnetosheath (top row) and magnetosphere (bottom row) density as determined using our automated region sorting method for the NIMF (left) and PSIMF (right) simulations are plotted as a function of simulation time in blue. For the duration of both simulations, these values match well with the known initial value in each region, shown in back.

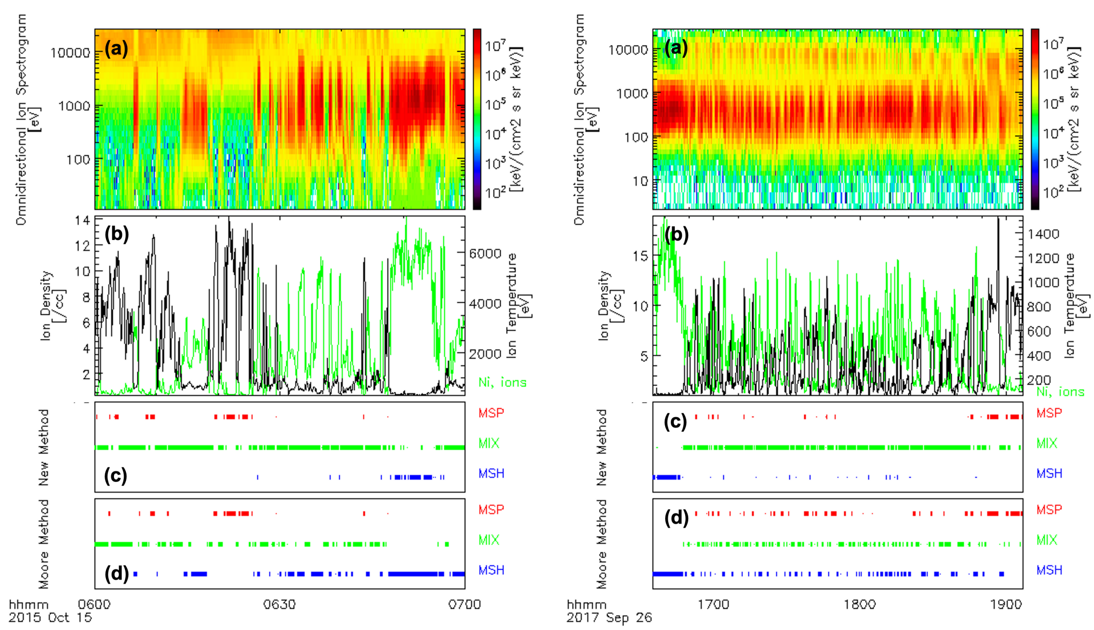

Figure 4. Omnidirectional ion energy (top), ion density and temperature (upper middle), regions as determined using the method developed in this study (lower middle), and regions as determined using methods presented in *Moore et al.* [2017] (bottom). The new region sorting method places more plasma in the mixed regions than the Moore method, but the results are comparable.

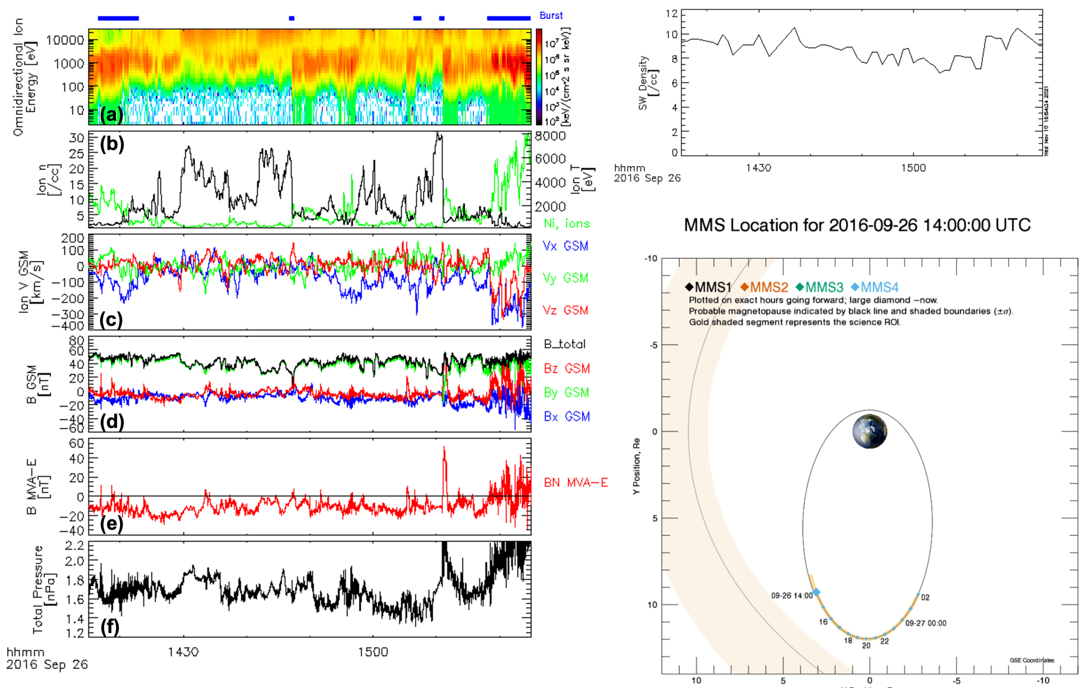

Figure 5. MMS observations of the KHI event on 26 September 2016. Solar wind density was high, between 8 and 10 /cc, pushing the magnetopause boundary further in than the approximation shown. MMS skimmed the magnetopause boundary, primarily on the magnetospheric side, with a brief excursion to the pure magnetosheath at the end of the inteval.

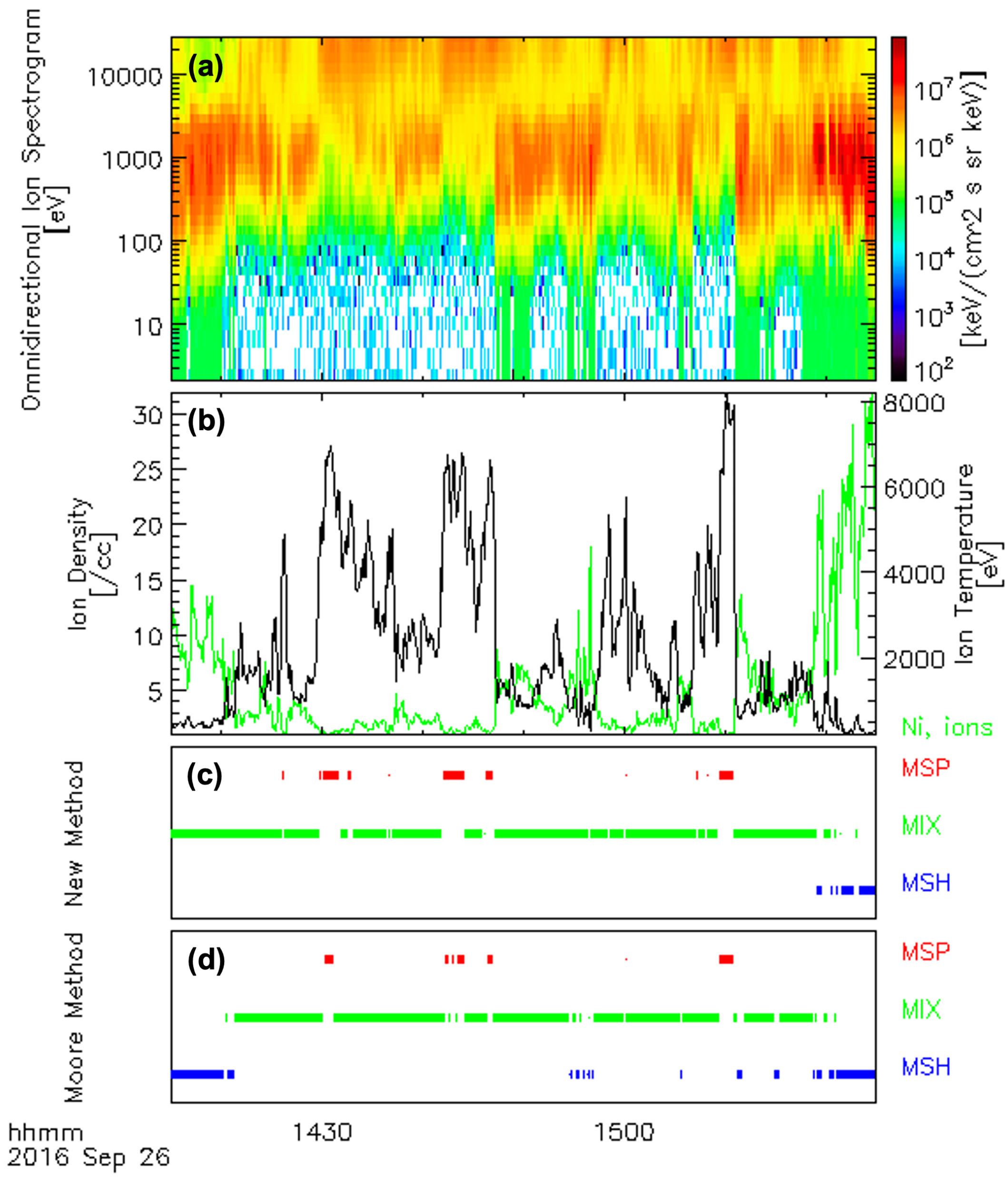

Figure 6. MMS observations of the KHI event on 26 September 2016 and the regions sorted using the new method presented in this paper and *Moore et al.* [2017]. SW density and MHD shock physics dictate a sheath density of ≈ 30 /cc, as is observed at the end of the interval. The new region sorting method corresponds well with this expectation, but the Moore method also identifies an earlier timespan with about half the expected sheath density. The new method is better at isolate only the pure sheath and sphere regions, resulting in more plasma being classified as "mixed."

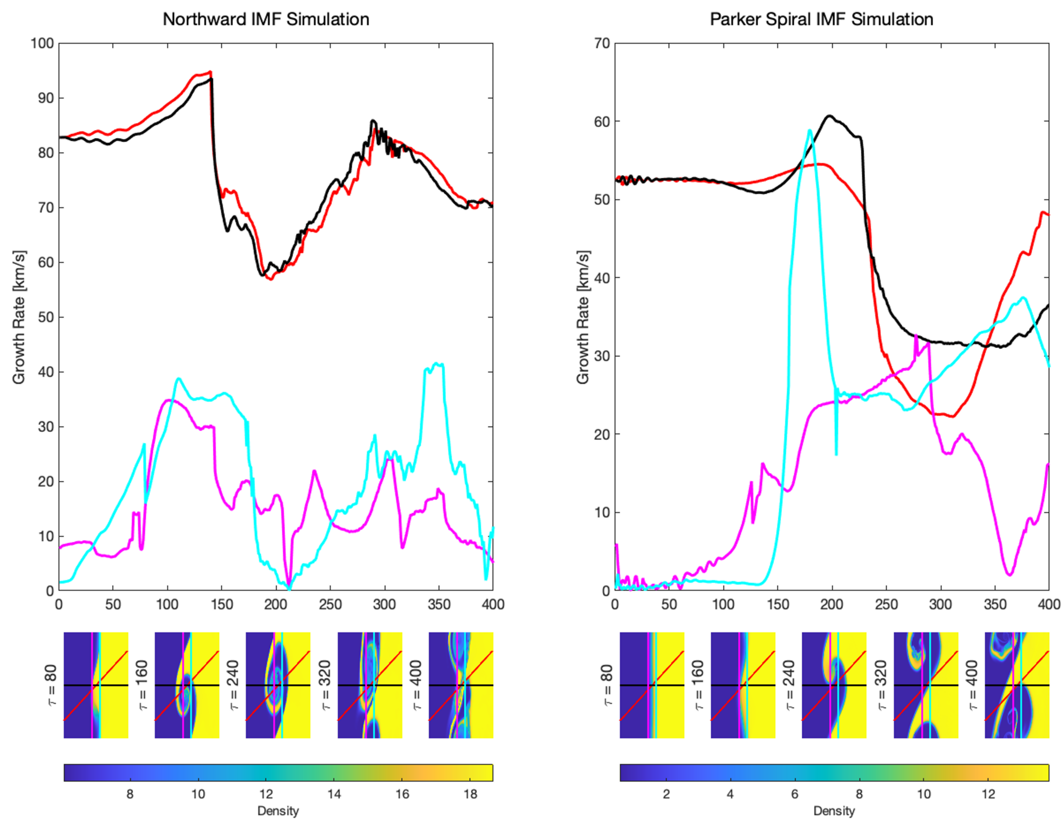

Figure 7. Cut geometry can have a significant effect on the growth rate. Cuts which spend nearly equal time on both sides of the boundary tend to have larger growth rates than cuts which merely skim the instability, spending significantly more time in one region than the other. For both the NIMF (left) and PSIMF (right) simulation, growth rates are calculated at each time step for the four cuts shown in the bottom panels. Colors in the growth rate plot correspond to the color of the cut shown in the simulation space.